Trabajo Fin de Máster

Máster en Diseño Avanzado en Ingeniería Mecánica

Criterios de Fallo en Modelos de Plasticidad en Policristales

Carmen Madrigal Sánchez

Director: Dr. Alfredo Navarro Robles

Universidad de Sevilla

Escuela Técnica Superior de Ingenieros Industriales

Diciembre, 2007

Este proyecto se basa en el trabajo realizado por la autora durante la estancia realizada en la Universidad de Oxford:

Material Failure in Crystal Plasticity Modelling

Author: Carmen Madrigal
Supervisor: Professor Fionn Dunne

Solid Mechanics and Materials Engineering Research Group
Department of Engineering Science
University of Oxford
December, 2007

Contents

Chapter 1

Introduction

Titanium alloys have been widely used in aerospace applications over the latter half of the 20th century. Corrosion resistance and reduced density represent some their advantages in comparison to steels, which dominated the early engine designs [Bache, 2003].

Capable of operating at elevated temperatures, near α and α/β titanium alloys are suitable for critical rotating components such as discs or blades, which experience demanding, principally cyclic loading conditions. Figure 1.1 illustrates the typical loading regimes for gas turbine components [Rugg et al., 2007].

Despite being in used for the last 50 years, significant gaps in our knowledge exist. The specific phenomenon of ambient temperature dwell sensitivity was first observed in 1972. It was shown that the introduction of a hold time at high mean stress could reduce the fatigue life of a component by over an order of magnitude [Bache et al., 1997]. Attempts to reproduce the relations between structure, texture and mechanical properties have not still been successful.

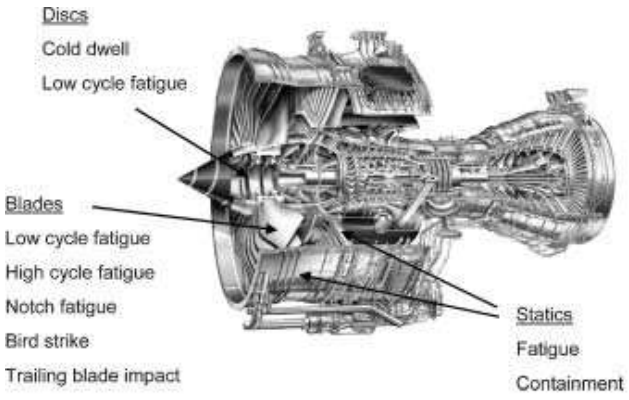

Figure 1.1: Loading regimes for critical parts in a gas turbine engine [Rugg et al., 2007].

However, it is becoming increasingly recognised that lifetime is dominated by *faceting*, that is, micro-crack development at a length of about the grain size, related to the probability of regions containing "weak" and "strong" crystallographic combinations.

Crystal plasticity is instrumental in understanding cold dwell fatigue and facet formation. Models of polycrystals containing sets of grains with particular lattice orientations permit systematic studies, aiming to explain the observed behaviour [Dunne et al., 2007b,c, Manonukul and Dunne, 2004].

The present work is conducted in partnership with Rolls-Royce plc, developed in the context of Ti alloys used for gas turbine components. Rolls-Royce has active programmes on crystal plasticity modelling. A physically-based,

lengthscale- and rate-dependent, elastically anisotropic crystal plasticity formulation, derived by Dunne et al. [2007a], implemented in the commercial FE package ABAQUS, is employed to further investigate crystallography effects and failure of the near α alloy Ti-6Al.

The crystal plasticity model is described in the following chapter of this report, followed by a description of its implementation into ABAQUS code, in Chapter 3. Crystallographic orientation effects are assessed in Chapter 4. In addition, lengthscale influence and its interaction with microstructure are analysed. Chapter 5 addresses failure under monotonic loading. Various criteria are proposed and predictions are contrasted with experimental data. Conclusions and further work are presented in the closing Chapter 6.

Chapter 2

Review and implementation of crystal plasticity for the uniaxial load case

This section briefly introduces the origins of yield and plastic flow. The classic concepts of crystal slip, slip systems and Schmid's law are reviewed. A physically-based, lengthscale- and rate-dependent, elastically anisotropic crystal plasticity formulation, derived by Dunne et al. [2007a], is subsequently addressed. The constitutive equations of this model are integrated under both explicit and implicit schemes for a uniaxial case. A comparison of the results is reported at the end of the section.

2.1 Crystal plasticity

The evidence of crystal slip being the origin of plasticity comes from mechanical tests carried out on single crystals of metals [Cottrell, 1949]. The

slip occurs on planes resulting from many hundreds of dislocations running through the crystal and emerging at the edge.

Observations on single crystals show that slip tends to occur preferentially on certain planes and in certain specific crystal directions. These tend to be the most densely packed planes or *slip planes*, and in the directions in which the atoms are packed closest together, or *slip directions* [Dunne and Petrinic, 2005].

2.2 Crystal slip in HCP near-alpha Ti-6Al

The alloy considered in the present work is the near-alpha titanium alloy Ti-6Al. It is mostly composed of single HCP α-phase, so that the BCC β-phase can be neglected.

There is some evidence that in these alloys, slip occurs predominantly on the basal [Williams et al., 2002] and prismatic [Neeraj et al., 2000, Suri et al., 1997] planes, since the resolved shear stress necessary to cause slip on the pyramidal plane is much higher than that on the other planes.

Assuming the inactivity of the pyramidal planes, the basal and prismatic slip planes and directions, shown in Fig. 2.1, define six slip systems, collected in Table 2.1.

2.2.1 Schmid's law

Schmid postulated that slip would take place in a given slip system, when the resolved shear stress τ, on the slip plane in the slip direction reached a critical value [Dunne and Petrinic, 2005]. When a single crystal is subjected

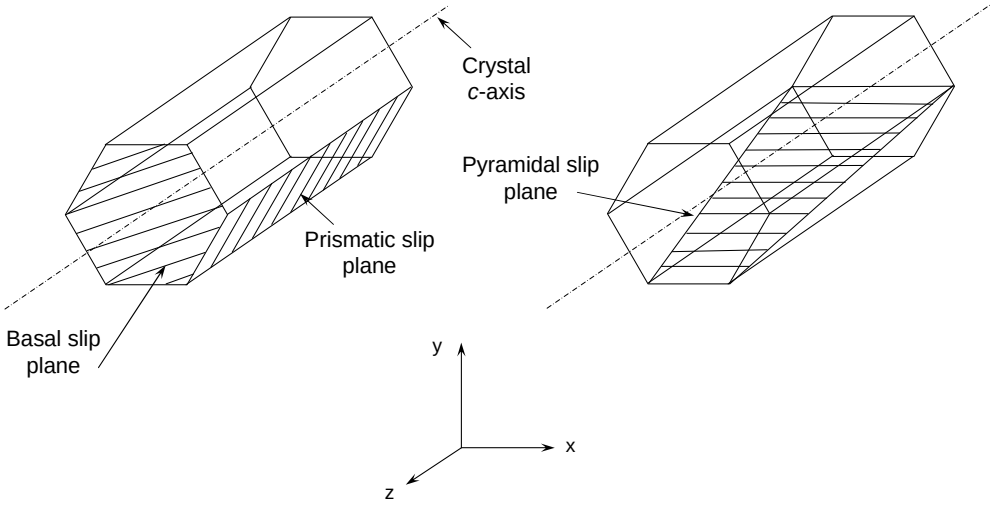

Figure 2.1: Schematic of the HCP unit cell showing the possible slip planes.

to a stress $\boldsymbol{\sigma}$, the shear stress component resolved on the slip plane of normal vector $\boldsymbol{n}$, in the slip direction $\boldsymbol{s}$ is given by

$$\tau = (\boldsymbol{\sigma}\boldsymbol{n}) \cdot \boldsymbol{s}. \tag{2.1}$$

Considering a uniaxial load applied in the direction $\boldsymbol{t}$, parallel to the y-axis, Figure 2.2, the stress can be written as follows:

$$\boldsymbol{\sigma} = \begin{pmatrix} 0 & 0 & 0 \\ 0 & \sigma_{22} & 0 \\ 0 & 0 & 0 \end{pmatrix}. \tag{2.2}$$

Basal	Prismatic
$\hat{\mathbf{s}}_1 = \frac{1}{2}\begin{pmatrix} 1 \\ -\sqrt{3} \\ 0 \end{pmatrix} \quad \hat{\mathbf{n}} = \begin{pmatrix} 0 \\ 0 \\ 1 \end{pmatrix}$	$\hat{\mathbf{s}}_1 = \frac{1}{2}\begin{pmatrix} 1 \\ -\sqrt{3} \\ 0 \end{pmatrix} \quad \hat{\mathbf{n}}_1 = \frac{1}{2}\begin{pmatrix} -\sqrt{3} \\ -1 \\ 0 \end{pmatrix}$
$\hat{\mathbf{s}}_2 = \begin{pmatrix} 1 \\ 0 \\ 0 \end{pmatrix} \quad \hat{\mathbf{n}} = \begin{pmatrix} 0 \\ 0 \\ 1 \end{pmatrix}$	$\hat{\mathbf{s}}_2 = \begin{pmatrix} 1 \\ 0 \\ 0 \end{pmatrix} \quad \hat{\mathbf{n}}_2 = \begin{pmatrix} 0 \\ -1 \\ 0 \end{pmatrix}$
$\hat{\mathbf{s}}_3 = \frac{1}{2}\begin{pmatrix} 1 \\ \sqrt{3} \\ 0 \end{pmatrix} \quad \hat{\mathbf{n}} = \begin{pmatrix} 0 \\ 0 \\ 1 \end{pmatrix}$	$\hat{\mathbf{s}}_3 = \frac{1}{2}\begin{pmatrix} 1 \\ \sqrt{3} \\ 0 \end{pmatrix} \quad \hat{\mathbf{n}}_3 = \frac{1}{2}\begin{pmatrix} \sqrt{3} \\ -1 \\ 0 \end{pmatrix}$

Table 2.1: HCP crystal basal and prismatic slip systems

Then the resolved shear stress can be calculated from Eq. 2.1:

$$\tau = \sigma_{22}\, n_2\, s_2, \tag{2.3}$$

or

$$\tau = \sigma_{22}\, \cos\phi\, \cos\lambda \equiv \sigma(\boldsymbol{t}\cdot\boldsymbol{n})(\boldsymbol{t}\cdot\boldsymbol{s}), \tag{2.4}$$

where ϕ and λ are the angles that the slip plane normal, $\boldsymbol{n}$, and slip direction, $\boldsymbol{s}$, form with the loading axis, respectively. The factor $\cos\phi\cos\lambda$ is known as the *Schmid factor*.

2.2.2 Crystal plasticity constitutive equations

In order to calculate the slip rate on the slip planes, a constitutive equation is required. Dunne et al. [2007a] derived a physically-based, lengthscale- and rate-dependent, elastically anisotropic crystal plasticity model, which is based upon dislocation glide and pinning.

Material hardening is considered to be controlled by the total density of dislocations, which includes statistically stored (SSDs), and geometrically nec-

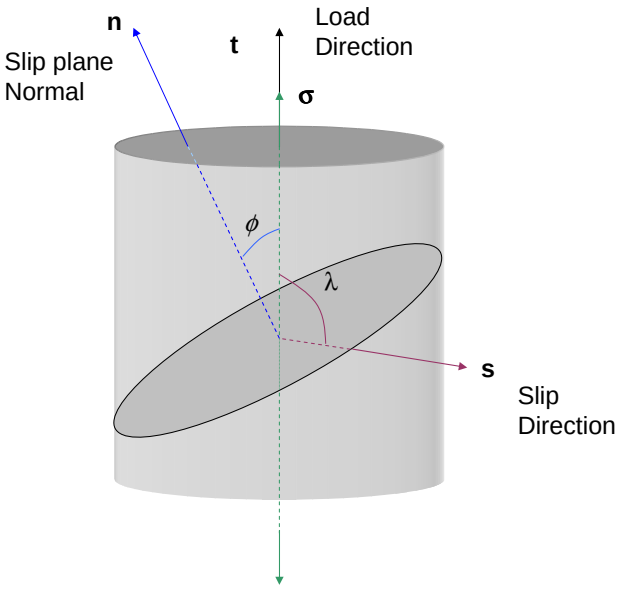

Figure 2.2: A single crystal containing a slip plane with normal $\boldsymbol{n}$ and slip direction $\boldsymbol{s}$, loaded in direction $\boldsymbol{t}$.

essary dislocations (GNDs). Both types are generated, move and are stored when a crystal is plastically deformed. However, the former are stored by trapping each other randomly while the latter are required for compatible non-uniform plastic deformation [Fleck et al., 1994]. GNDs do not contribute to plastic strain because of their sessile nature, but induce additional hardening by hindering the movement of mobile SSDs [Gao and Huang, 2003].

Plastic strain gradients may arise because of the geometry of the loading or because of the inhomogeneity of the material itself. Thus, the mismatch of slip bands at the grain boundaries or the presence of hard, non-deforming particles generate gradients of plastic strain with subsequent formation of GNDs leading to gradient strain hardening.

According to Dunne et al. [2007a], the plastic velocity gradient is given by

$$\boldsymbol{L}^{\mathrm{p}} = \sum_{\kappa} \rho\, b^2 \nu \exp\left(-\frac{\Delta F}{kT}\right) \sinh\left(\frac{(\tau^{\kappa} - \tau_{\mathrm{c}} - r)b^2}{kT\sqrt{\rho + \rho_{\mathrm{G}}}}\right) \boldsymbol{s}^{\kappa} \otimes \boldsymbol{n}^{\kappa}, \tag{2.5}$$

on the basis of planar slip occurring through release and pinning of gliding, statistically stored dislocations with density ρ and an activation energy ΔF. ν is the frequency of attempts, successful or otherwise, of dislocations to jump energy barriers; k the Boltzman constant; T the absolute temperature; τ^{κ} the resolved shear stress on system κ; τ_{c} the critical resolved shear stress and $\boldsymbol{s}^{\kappa}$ and $\boldsymbol{n}^{\kappa}$ are the direction and normal associated with the κth slip system, respectively. The activation volume is $b^2 l$, where l is the mean free distance between dislocations, $l = 1/\sqrt{\rho + \rho_{\mathrm{G}}}$, and b the Burger's vector magnitude.

The density of GNDs is geometrically dependent, thus giving rise to a lengthscale-dependent slip rule. Busso et al. [2000] showed that the incremental evolution of ρ_{G} on the κth slip plane with normal $\boldsymbol{n}$ may be written as

$$\Delta\boldsymbol{\rho}_{\mathrm{G}}^{\kappa} = \frac{\Delta\gamma^{\kappa}}{b}\mathrm{curl}[\boldsymbol{n}^{\kappa}\boldsymbol{F}^{\mathrm{p}}], \tag{2.6}$$

where the slip rate, $\Delta\gamma^{\kappa}$, is given by Eq. 2.5, taking into account that

$$\boldsymbol{L}^{\mathrm{p}} = \sum_{\kappa} \dot{\gamma}^{\kappa} \boldsymbol{s}^{\kappa} \otimes \boldsymbol{n}^{\kappa}.$$

GNDs on the κth slip system can be represented as the screw dislocation line segments parallel to the slip direction $\boldsymbol{s}$, and the edge dislocation line segments having directions in the plane normal $\boldsymbol{n}$ and directions $\boldsymbol{m}$ ($\boldsymbol{m} = \boldsymbol{s} \times \boldsymbol{n}$), such that

$$\sum_{\kappa}(\Delta\rho_{\mathrm{en}}^{\kappa}\boldsymbol{n} + \Delta\rho_{\mathrm{em}}^{\kappa}\boldsymbol{m} + \Delta\rho_{\mathrm{s}}^{\kappa}\boldsymbol{s}) = \sum_{\kappa}\Delta\boldsymbol{\rho}_{\mathrm{G}}^{\kappa} = \sum_{\kappa}\Delta\boldsymbol{\rho}_{\mathrm{G}}, \tag{2.7}$$

where the densities developing on all the active slip systems are summed up and assumed to exist on all slip systems. In doing so, the influence of the active slip system on the hardening of the inactive slip systems, that is, latent hardening, is included in a simple way.

The the slip-resistance contribution due to SSDs is included by means of a strain hardening parameter r, whose evolutionary law is assumed linear. The increment of r is proportional to the accumulated plastic strain increment,

$$\Delta r = h\Delta p, \tag{2.8}$$

where h is a constant and the accumulated slip rate, $\dot{p}$, is given by

$$\dot{p} = \sqrt{\frac{2}{3}\boldsymbol{L}^{\mathrm{p}} : \boldsymbol{L}^{\mathrm{p}}}.$$

2.3 Implicit and explicit integration

Implicit finite-element methods are considerably robust and can prove advantageous when the stress and deformation paths remain nearly proportional. Under these conditions, implicit methods can significantly speed up the calculations by enabling the use of larger time steps than otherwise permitted by their explicit counterpart [Cuitiño and Ortiz, 1993]. On the other hand, the number of iterations required to solve a stiff set of equations may be considerably large [Kuchnicki et al., 2006].

This section describes the implementation of the crystal plasticity model introduced above, using both explicit and implicit formulations. In order to do so, a single HCP unit cell, subjected to a uniaxial load is considered. A strain parallel to the y-axis is applied, at a constant strain rate, during a certain time period. The crystal position is established to be the reference configuration described in Section 2.2, Table 2.1.

2.3.1 Explicit Formulation

Given a time increment, Δt, and a strain rate, $\dot{\varepsilon}$, the stress and strain at the end of the interval are

$$\begin{aligned} \sigma_{(t+1)} &= \sigma_{(t)} + \dot{\sigma}\Delta t \quad \text{and} \\ \varepsilon_{(t+1)} &= \varepsilon_{(t)} + \dot{\varepsilon}\Delta t, \end{aligned}$$

where

$$\dot{\sigma} = E(\dot{\varepsilon} - \dot{\varepsilon}^{\mathrm{p}}). \tag{2.9}$$

The plastic strain rate, $\dot{\varepsilon}^{\mathrm{p}}$ in Eq. 2.9, is calculated from the proposal of Dunne et al. [2007a], reduced for one dimension:

$$\dot{\varepsilon}^{\mathrm{p}} = \sum_{\kappa} \alpha \sinh(\beta(\tau^{\kappa} - \tau_{\mathrm{c}}))s^{\kappa}n^{\kappa}, \tag{2.10}$$

in which α and β are just groupings of the material properties given in Eq. 2.5, while n^{κ} and s^{κ} are the components of the normal and slip directions in the y-axis, respectively. The resolved shear stress is given by Schmid's law, Eq. 2.3.

It is important to notice that $\dot{\varepsilon}^{\mathrm{p}}$ is taken as the plastic strain rate at the end of the previous time increment and it is assumed constant. This fact precludes large time increments, as in this case, the calculated stress would not be accurate enough. In this analysis, the loading history is divided into 1000 steps.

The material properties arising in Eq. 2.9 are collected in Table 2.2. The critical resolved shear stress, τ_{c}, and the Helmholtz free energy, ΔF, represent the macroscale, uniaxial, rate-dependent stress-strain response of the titanium alloy at room temperature, [Hasija et al., 2003]. The density of the GNDs is not updated, so that strain hardening is not activated. On the other hand, Schmid's law predicts first slip on the first and third prismatic slip planes, at a stress level of 600.4 MPa.

τ_c [MPa]	b [m]	k [JK^{-1}]	ΔF [J]
260	2.5×10^{-10}	1.38×10^{-23}	11.71×10^{-20}

ν [s^{-1}]	ρ [m^{-2}]	ρ_{G0} [m^{-2}]
5.0×10^{19}	1.0×10^{10}	23.9×10^{3}

Table 2.2: Material properties of alloy Ti-6Al at room temperature

The stress obtained is plotted against the total strain in Figure 2.3. The yield point is observed at around 600 MPa, matching the expected value. Furthermore, no hardening is shown in the plastic period, proving the legitimacy of this approach.

2.3.2 Implicit Formulation

The implicit formulation implemented here is that followed by Dunne et al. [2007a], except for it has been specialised for just one dimension. This has been done by simply substituting the tensor and vector quantities by the appropriate component. In this study, an imposed deformation is applied along the y-axis. Therefore, the only components of interest are σ_{22} and ε_{22}. In what follows, the subscripts have been eliminated for expediency. Moreover, all quantities are written at the end of the time increment, unless explicitly specified otherwise, so that $\sigma_{(t+\Delta t)}$, will be referred to as σ.

The stress may be expressed in terms of a trial stress, σ^{tr}, which considers the deformation to be entirely elastic, and afterwords modified by a plastic corrector term

$$\sigma = E\varepsilon^{\mathrm{e}} = E(\varepsilon^{\mathrm{e}}_{(\mathrm{t})} + \Delta\varepsilon^{\mathrm{e}}) = E(\varepsilon^{\mathrm{e}}_{(\mathrm{t})} + \Delta\varepsilon) - E\Delta\varepsilon^{\mathrm{p}} = \sigma^{\mathrm{tr}} - E\Delta\varepsilon^{\mathrm{p}}. \quad (2.11)$$

The implicit scheme is carried out by means of a Newton-type algorithm, which is performed until a specified residual tolerance is achieved. This

residual is defined as

$$\Psi = \sigma - \sigma^{\mathrm{tr}} + E\Delta\varepsilon^{\mathrm{p}} = 0, \tag{2.12}$$

which differentiated gives

$$\delta\Psi = \delta\sigma - \delta\sigma^{\mathrm{tr}} + E\delta\Delta\varepsilon^{\mathrm{p}} = 0. \tag{2.13}$$

The differential of the plastic strain increment, $\delta\Delta\varepsilon^{\mathrm{p}}$, is again calculated from Dunne's model, which for one dimension takes the form of Eq. 2.10, so

$$\begin{aligned} \delta\Delta\varepsilon^{\mathrm{p}} &= \delta\left(\sum_{\kappa}\alpha\sinh(\beta(\tau^{\kappa}-\tau_{\mathrm{c}}))\Delta t s^{\kappa}n^{\kappa}\right) \\ &= \sum_{\kappa}\alpha\beta\cosh(\beta(\tau^{\kappa}-\tau_{\mathrm{c}}))\Delta t s^{\kappa}n^{\kappa}\delta\tau^{\kappa}, \end{aligned} \tag{2.14}$$

in which α and β are just groupings of the material properties given in Eq. 2.5, while n^{κ} and s^{κ} are the components in the y-axis of the normal and slip directions respectively.

In order to obtain $\delta\tau^{\kappa}$, Schmid's law for the uniaxial case, Eq. 2.3, is differentiated

$$\delta\tau^{\kappa} = \delta\sigma s^{\kappa}n^{\kappa}. \tag{2.15}$$

Introducing then Eq. 2.15 into Eq. 2.14 one obtains

$$\delta\Delta\varepsilon^{\mathrm{p}} = \sum_{\kappa}\alpha\beta\cosh(\beta(\tau^{\kappa}-\tau_{\mathrm{c}}))\Delta t(s^{\kappa}n^{\kappa})^2\delta\sigma \equiv P\delta\sigma, \tag{2.16}$$

which substituted into Eq. 2.13 gives

$$\delta\Psi = \delta\sigma - \delta\sigma^{\mathrm{tr}} + EP\delta\sigma = [1+EP]\delta\sigma, \tag{2.17}$$

as σ^{tr} is fixed during the iteration.

Newton algorithm scheme states that

$$\Psi + \frac{\partial\Psi}{\partial\sigma}\delta\sigma = [\sigma - \sigma^{\mathrm{tr}} + E\Delta\varepsilon^{\mathrm{p}}] + [1+EP]\delta\sigma = 0,$$

so the stress can be updated iteratively by

$$\delta\sigma = [1 + EP]^{-1} \left\{ \sigma - \sigma^{\mathrm{tr}} + E \left(\sum_{\kappa} \alpha \sinh(\beta(\tau^{\kappa} - \tau_{\mathrm{c}})) \Delta t s^{\kappa} n^{\kappa} \right) \right\},$$

with

$$\sigma^{(n+1)} = \sigma^{(n)} + \delta\sigma,$$

until the specified tolerance is reached

$$|\Phi| = |\sigma - \sigma^{\mathrm{tr}} + E\Delta\varepsilon^{\mathrm{p}}| \leq 10^{-12}$$

As mentioned before, this procedure permits a larger time increment to be employed, which means that the total strain may be applied in only a few steps. Therefore, this simulation has been implemented for 1000, 100 and just 10 time increments, resulting in identical values of stress and strain. The stress-strain curves, obtained from the implicit integration, lay over that from the explicit scheme, as depicted in Figure 2.3.

It may be concluded, therefore, that both schemes provide satisfactory solutions, which fit the theoretical values. In addition, the advantages of the implicit integration are proved by setting a time increment up to ten times longer.

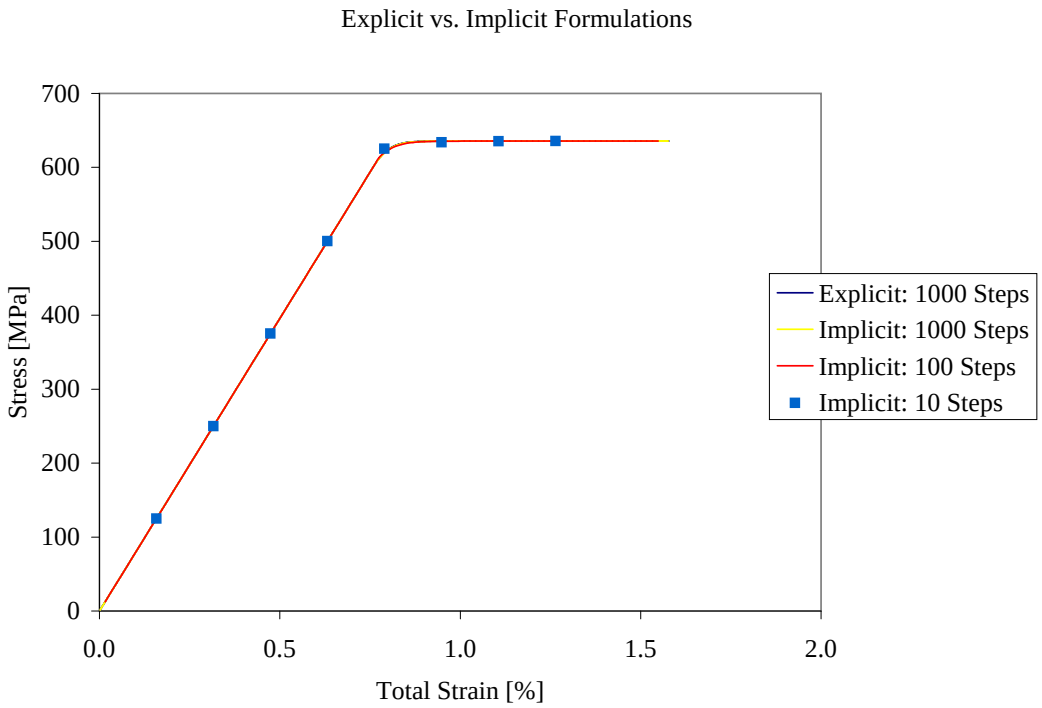

Figure 2.3: Implementation of crystal plasticity for the uniaxial loading case. Comparison between implicit and explicit formulations. (The curves plotted in solid lines overwrite one another)

Chapter 3

Implementation of crystal plasticity into FE code

The implementation of crystal plasticity into numerical analysis is done by means of an ABAQUS-Standard user-defined finite element subroutine (UEL). This section gives a summary of the finite element implicit integration algorithm and how it is transferred into ABAQUS.

3.1 Finite Element implicit integration scheme

A Finite Element implicit integration is based on a residual, $\boldsymbol{r}$, defined as the difference between the internal and external forces applied to the system [Zienkiewicz, 1977, Fenner, 1975], such that

$$\boldsymbol{r} = \boldsymbol{f}^{\text{int}} - \boldsymbol{f}^{\text{ext}}.$$

A Newton iteration is performed until a specified tolerance is reached. The

displacements are then updated according to:

$$\boldsymbol{r} + \frac{\partial \boldsymbol{r}}{\partial \boldsymbol{u}} \Delta \boldsymbol{u} = 0 \quad \Rightarrow \quad \Delta \boldsymbol{u} = - \left[\frac{\partial \boldsymbol{r}}{\partial \boldsymbol{u}} \right]^{-1} \boldsymbol{r} \quad \Rightarrow \quad \boldsymbol{u}^{(n+1)} = \boldsymbol{u}^{(n)} + \Delta \boldsymbol{u}.$$

Furthermore, in the absence of external forces, the residual vector equals the internal force vector, which may be expressed as

$$\boldsymbol{r} = \boldsymbol{f}^{\text{int}} = \int \boldsymbol{B}^{\text{T}} \boldsymbol{\sigma} \text{d}V = \int \boldsymbol{B}^{\text{T}} \left[\boldsymbol{\sigma}_t + \boldsymbol{C}^{\text{ep}} \Delta \boldsymbol{\varepsilon} \right] \text{d}V, \tag{3.1}$$

where the stress has been written in terms of the elastic-plastic tangent stiffness matrix, $\boldsymbol{C}^{\text{ep}}$, and the stress at the beginning of a given time increment, $\boldsymbol{\sigma}_t$.

Differentiating this equation and taking into account that $\boldsymbol{\varepsilon} = \boldsymbol{B}\boldsymbol{u}$, gives

$$\delta \boldsymbol{f}^{\text{int}} = \int \boldsymbol{B}^{\text{T}} \left[\delta \boldsymbol{\sigma}_t + \boldsymbol{C}^{\text{ep}} \delta \Delta \boldsymbol{\varepsilon} \right] \text{d}V = \int \boldsymbol{B}^{\text{T}} \boldsymbol{C}^{\text{ep}} \boldsymbol{B} \text{d}V \delta \boldsymbol{u},$$

so the Jacobian may be finally be obtained from

$$\boldsymbol{J} = \frac{\partial \boldsymbol{f}^{\text{int}}}{\partial \boldsymbol{u}} = \int \boldsymbol{B}^{\text{T}} \boldsymbol{C}^{\text{ep}} \boldsymbol{B} \text{d}V. \tag{3.2}$$

It may be concluded, therefore, that both the residual, $\boldsymbol{r}$, and its Jacobian, $\boldsymbol{J} = \partial \boldsymbol{r} / \partial \boldsymbol{u}$, are necessary in order to solve the boundary value problem, which implies the knowledge of the consistent elastic-plastic tangent stiffness matrix, addressed in Section 3.2.1.

In this 3D scheme, an isoparametric element is defined by quadratic shape functions, $\boldsymbol{N}$, such that $\boldsymbol{x} = \boldsymbol{N}(\boldsymbol{\xi}) \boldsymbol{x}^{\text{N}}$, with $\boldsymbol{\xi} = [\nu, \eta, \xi]$. Thus, the volume differential is expressed as

$$\text{d}V = t \det(\boldsymbol{J}) \text{d}\nu \text{d}\eta \text{d}\xi,$$

where t is the element thickness and $\boldsymbol{J}$ the Jacobian of the transformation, $\boldsymbol{J} = \partial \boldsymbol{x} / \partial \boldsymbol{\xi}$.

In this way, the integrals of Eq. 3.1 and 3.2, are approximated as

$$\boldsymbol{f}^{\text{int}} = t \int\int\int \boldsymbol{B}^{\text{T}}\boldsymbol{\sigma}\det(\boldsymbol{J})\mathrm{d}\nu\mathrm{d}\eta\mathrm{d}\xi \approx t\sum_{i=1}^{2}\sum_{j=1}^{2}\sum_{k=1}^{2} H_i H_j H_k \boldsymbol{B}^{\text{T}}\boldsymbol{\sigma}\det(\boldsymbol{J}), \tag{3.3}$$

$$\boldsymbol{J} = t \int\int\int \boldsymbol{B}^{\text{T}}\boldsymbol{C}^{\text{ep}}\boldsymbol{B}\mathrm{d}\nu\mathrm{d}\eta\mathrm{d}\xi \approx t\sum_{i=1}^{2}\sum_{j=1}^{2}\sum_{k=1}^{2} H_i H_j H_k \boldsymbol{B}^{\text{T}}\boldsymbol{C}^{\text{ep}}\boldsymbol{B}\det(\boldsymbol{J}), \tag{3.4}$$

where H_n, $n = i, j, k$ are the Gauss integration weighting values at the integration points.

3.2 Commercial FE package ABAQUS

The implementation of user-defined materials into ABAQUS is usually done by means of the user-defined material subroutine, (UMAT). This code computes the stress at each integration point at the end of the increment while ABAQUS performs the remaining calculations. However, the crystal plasticity model, described in Chapter 2, is based on the density of GNDs, which necessitates the knowledge of the spatial gradients of the plastic deformation gradients. This spatial gradient is calculated from the plastic deformation at all the integration points of a given element. For this reason, a more general subroutine is used, which includes the state of the whole element. The ABAQUS-Standard user-defined finite element subroutine, (UEL), fulfils this condition.

Thus, a user-defined 20-noded, reduced integration element subroutine is developed. For each element specified as user-defined, ABAQUS calls this subroutine when the element Jacobian or stiffness matrix and the element residuals are required. The Gaussian integration rules, the shape functions and the model integration scheme should be therefore defined in this subroutine. In this way, ABAQUS is essentially used to solve the overall system of equations.

An array containing the solution dependent state variables at the start of the current increment is passed into the UEL. These quantities are updated to be the values at the end of the increment. However, as the state variables are assembled into an array for the entire element, ABAQUS is not able to generate spatial contour plots for them.

In order to view the results, an auxiliary mesh, with matching nodes, integration points and elements is laid on top of the model mesh. This auxiliary mesh is purely needed for visualisation purposes. The state dependent variables computed by the UEL subroutine for each element are assigned to the overlay element by means of a user defined material subroutine (UMAT), which supports visualisation.

The function of a UMAT is to define the material behaviour. This subroutine is provided with the strains at each integration point in order to update the stresses and the solution dependent state variables to the values at the end of the increment. Moreover, it must return the material Jacobian matrix, $\delta\Delta\sigma/\delta\Delta\varepsilon$. For the UMAT assigned to the fictitious mesh, both the stresses and the material Jacobian matrix are assigned null values so as not to have any influence on the boundary value problem. The state variables are then transferred from the UEL subroutine for each integration point.

Each time the UEL solves an element, the updated state variables are stored in a common block, which is accessible to all subroutines. Then, when the UMAT is called for each integration point of the overlay mesh, the variables are extracted from the common block, so they can be plotted.

In addition, along with the code defining the subroutines, ABAQUS requires an input file in which the boundary value problem is defined. The two meshes, the boundary and loading conditions, the output requests and the properties of each user defined element are included in this file.

A more detailed description of the UEL subroutine is given in the following section.

3.2.1 UEL algorithm

As mentioned earlier, this routine is aimed to calculate the spatial gradient of the plastic deformation gradient, (curl[$\boldsymbol{F}^{\mathrm{p}}$]), so that the consistent elastic-plastic tangent stiffness matrix may be obtained.

In order to determine this, an internal, eight-noded, linear element is introduced within each eight-noded element, such that the nodes of the former coincide with the Gauss points of the later [Dunne et al., 2007a, Busso et al., 2000]. The spatial derivatives may be then obtained from

$$\frac{\partial \boldsymbol{F}^{\mathrm{p}}}{\partial \boldsymbol{x}} = \frac{\partial}{\partial \boldsymbol{x}} \left(\boldsymbol{n} \boldsymbol{F}_i^{\mathrm{p}} \right) = \frac{\partial \boldsymbol{n}}{\partial \boldsymbol{x}} \boldsymbol{F}_i^{\mathrm{p}} = \frac{\partial \boldsymbol{n}}{\partial \boldsymbol{\alpha}} \boldsymbol{J}^{-1} \boldsymbol{F}_i^{\mathrm{p}},$$

in which $\boldsymbol{n}(\boldsymbol{\alpha})$ are the linear shape functions, $\boldsymbol{J}$ the appropriate Jacobian transformation mapping from the external to the internal elements, and $\boldsymbol{F}_i^{\mathrm{p}}$ the plastic deformation gradients at each integration point.

Finally, the contribution of a given element to the residual vector, and the Jacobian of the overall system of equations are approximated by Eq. 3.3 and 3.4 and returned to the main program. In order to obtain the updated stress and the consistent elastic-plastic tangent stiffness matrix, the integration of the constitutive equation needs to be performed as described next.

Implicit integration of the constitutive equations. The implicit integration of the constitutive equations is carried out by means of a Newton-type algorithm, which is performed until a specified residual tolerance is achieved.

The stress is expressed in terms of a trial stress, $\boldsymbol{\sigma}^{\mathrm{tr}}$, which considers the deformation to be entirely elastic, and afterwords modified by a plastic corrector term

$$\boldsymbol{\sigma} = \boldsymbol{D}\boldsymbol{\varepsilon}^{\mathrm{e}} = \boldsymbol{D}\left(\boldsymbol{\varepsilon}_{(\mathrm{t})}^{\mathrm{e}} + \Delta\boldsymbol{\varepsilon}^{\mathrm{e}}\right) = \boldsymbol{D}\left(\boldsymbol{\varepsilon}_{(\mathrm{t})}^{\mathrm{e}} + \Delta\boldsymbol{\varepsilon}\right) - \boldsymbol{D}\Delta\boldsymbol{\varepsilon}^{\mathrm{p}} = \boldsymbol{\sigma}^{\mathrm{tr}} - \boldsymbol{D}\Delta\boldsymbol{\varepsilon}^{\mathrm{p}}, \quad (3.5)$$

in which $\boldsymbol{D}$ is the global elastic stiffness matrix determined from the local stiffness $\boldsymbol{C}$ by

$$\boldsymbol{D} = \boldsymbol{T}_{\sigma}^{-1}\boldsymbol{C}\boldsymbol{T}_{\varepsilon},$$

where $\boldsymbol{T}_{\sigma}$ and $\boldsymbol{T}_{\varepsilon}$ are the rotation matrices mapping the reference crystal coordinate system into the local one for each particular grain orientation, detailed in Dunne et al. [2007a].

The residual is then defined as

$$\boldsymbol{\Psi} = \boldsymbol{\sigma} - \boldsymbol{\sigma}^{\mathrm{tr}} + \boldsymbol{D}\Delta\boldsymbol{\varepsilon}^{\mathrm{p}} = 0, \tag{3.6}$$

and differentiated to give

$$\delta\boldsymbol{\Psi} = \delta\boldsymbol{\sigma} - \delta\boldsymbol{\sigma}^{\mathrm{tr}} + \boldsymbol{D}\delta\Delta\boldsymbol{\varepsilon}^{\mathrm{p}} = 0. \tag{3.7}$$

The differential of the plastic strain tensor increment, $\delta\Delta\boldsymbol{\varepsilon}^{\mathrm{p}}$, described in Chapter 2, is calculated from

$$\begin{aligned} \delta\Delta\boldsymbol{\varepsilon}^{\mathrm{p}} &= \delta\mathrm{sym}\left(\sum_{\kappa}\alpha\sinh\beta(\tau^{\kappa}-\tau_{\mathrm{c}})\Delta t\boldsymbol{s}^{\kappa}\otimes\boldsymbol{n}^{\kappa}\right), \\ &= \mathrm{sym}\left(\sum_{\kappa}\alpha\beta\cosh\beta(\tau^{\kappa}-\tau_{\mathrm{c}})\Delta t\boldsymbol{s}^{\kappa}\otimes\boldsymbol{n}^{\kappa}\delta\tau^{\kappa}\right), \end{aligned} \tag{3.8}$$

in which α and β are just groupings of the material properties given in Eq. 2.5, $\boldsymbol{n}^{\kappa}$ and $\boldsymbol{s}^{\kappa}$ are the the normal and slip directions respectively, and $\delta\tau^{\kappa}$ is given by

$$\delta\tau^{\kappa} = \delta(\boldsymbol{\sigma}\boldsymbol{n}^{\kappa})\cdot\boldsymbol{s}^{\kappa} \equiv (\boldsymbol{n}^{\kappa}\otimes\boldsymbol{s}^{\kappa}) : \delta\boldsymbol{\sigma}. \tag{3.9}$$

Introducing then Eq. 3.9 into Eq. 3.8 with all tensors written in Voigt notation,

$$\delta\Delta\boldsymbol{\varepsilon}^{\mathrm{p}} = \sum_{\kappa}\alpha\beta\cosh\beta(\tau^{\kappa}-\tau_{\mathrm{c}})\Delta t(\boldsymbol{A}^{\kappa}\otimes\boldsymbol{A}^{\kappa})\delta\boldsymbol{\sigma} = \boldsymbol{P}\delta\boldsymbol{\sigma}, \tag{3.10}$$

in which $\boldsymbol{A}^{\kappa} = \boldsymbol{s}^{\kappa}\otimes\boldsymbol{n}^{\kappa}$.

Substituting Eq. 3.10 into Eq. 3.7 gives

$$\delta\boldsymbol{\Psi} = \delta\boldsymbol{\sigma} - \delta\boldsymbol{\sigma}^{\mathrm{tr}} + \boldsymbol{D}\boldsymbol{P}\delta\boldsymbol{\sigma} = [\boldsymbol{I} + \boldsymbol{D}\boldsymbol{P}]\delta\boldsymbol{\sigma}. \tag{3.11}$$

Newton algorithm scheme states that

$$\boldsymbol{\Psi} + \frac{\partial\boldsymbol{\Psi}}{\partial\boldsymbol{\sigma}}\delta\boldsymbol{\sigma} = [\boldsymbol{\sigma} - \boldsymbol{\sigma}^{\mathrm{tr}} + \boldsymbol{D}\Delta\boldsymbol{\varepsilon}^{\mathrm{p}}] + [\boldsymbol{I} + \boldsymbol{D}\boldsymbol{P}]\delta\boldsymbol{\sigma} = 0,$$

so the stress can be updated iteratively by

$$\delta\boldsymbol{\sigma} = [\boldsymbol{I} + \boldsymbol{D}\boldsymbol{P}]^{-1}\left\{\boldsymbol{\sigma} - \boldsymbol{\sigma}^{\mathrm{tr}} + \boldsymbol{D}\mathrm{sym}\left(\sum_{\kappa}\alpha\sinh\beta(\tau^{\kappa} - \tau_{\mathrm{c}})\Delta t\boldsymbol{A}^{\kappa}\right)\right\},$$

with

$$\boldsymbol{\sigma}^{(n+1)} = \boldsymbol{\sigma}^{(n)} + \delta\boldsymbol{\sigma},$$

until the specified tolerance is reached

$$|\boldsymbol{\Psi}| = |\boldsymbol{\sigma} - \boldsymbol{\sigma}^{\mathrm{tr}} + \boldsymbol{D}\Delta\boldsymbol{\varepsilon}^{\mathrm{p}}| \leq 10^{-12}.$$

When this algorithm is completed, the consistent elastic-plastic tangent stiffness matrix is finally determined.

Consistent elastic-plastic tangent stiffness matrix. From the definition of the trial stress in Eq. 3.5,

$$\delta\boldsymbol{\sigma} = \delta\boldsymbol{\sigma}^{\mathrm{tr}} + \boldsymbol{D}\delta\Delta\boldsymbol{\varepsilon}^{\mathrm{p}} \tag{3.12}$$

In addition, the differential of the trial stress over the increment is

$$\delta\boldsymbol{\sigma}^{\mathrm{tr}} = \delta\left[\boldsymbol{D}\left(\boldsymbol{\varepsilon}^{\mathrm{e}}_{(t)} + \Delta\boldsymbol{\varepsilon}\right)\right] \equiv \boldsymbol{D}\delta\boldsymbol{\varepsilon}. \tag{3.13}$$

Introducing Eq. 3.10 and 3.13 into Eq. 3.12, the consistent elastic-plastic tangent stiffness matrix is finally given by

$$\boldsymbol{C}^{\mathrm{ep}} = \frac{\partial\boldsymbol{\sigma}}{\partial\boldsymbol{\varepsilon}} = [\boldsymbol{I} + \boldsymbol{D}\boldsymbol{P}]^{-1}\boldsymbol{D}. \tag{3.14}$$

3.3 Verification of the code

In order to ensure correct implementation into the code, a simple problem is simulated. An elastically isotropic model of only two grains with specific lattice orientations each is loaded in tension. Depending on the arrangement of the grains and their orientations, dissimilar evolutions of the local strain and stress are expected.

3.3.1 Test 1: Horizontal arrangement

The first test consists of a 3D plate composed of two adjacent grains of 2500 elements each. The bottom, left and back surfaces are constricted in the y-, x- and z-directions respectively. A uniform, ramp-type displacement is applied to the top surface nodes. In such an arrangement, both grains experience the same amount of total strain. A sketch of the model is depicted in Figure 3.1.

The orientation of the unit cell of the left grain corresponds to the reference configuration shown in Figure 2.1. Conversely, the right grain is rotated 90° around the x-axis such that its c-axis is parallel to the loading direction. In doing so, this grain becomes a hard or a badly oriented grain, since much higher stress is required to activate any of its slip systems, in comparison with a soft grain such as the left grain, whose c-axis is normal to the load. Furthermore, the density of the GNDs is set constant, so that no strain hardening is expected after the stress has stabilised. For the left grain, the Schmid's Law, Eq. 2.1, predicts a yield stress of 600.4 MPa and the constitutive equations integration scheme, developed in Chapter 2, gives a final stress value 635.52 MPa. However, the right grain is not likely to slip, as the load is perpendicular to the slip direction.

The results of the simulation are collected in Figure 3.2. The soft grain shows a perfect plastic behaviour with a yield point at around 600 MPa and

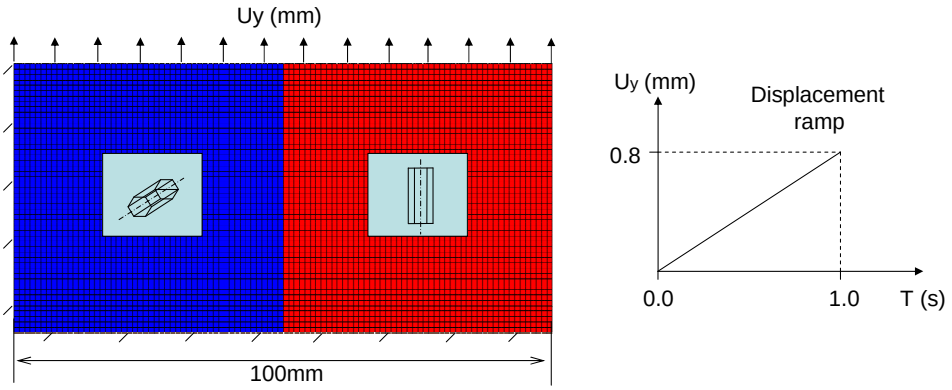

Figure 3.1: Verification of the code: hard and soft grains in horizontal arrangement.

a stabilized stress of 635.66 MPa, which fit the predicted values. On the contrary, the hard grain stays elastic at all load stages.

3.3.2 Test 2: Vertical arrangement

In the second test, the grains are rearranged in a vertical pile such as shown in Figure 3.3. The boundary conditions, the load and the density of GNDs are similar to those of the previous test. Regarding the orientation of the grains, the lower one coincides with the reference configuration, thus being soft, while the upper one is rotated 90°, thus becoming hard.

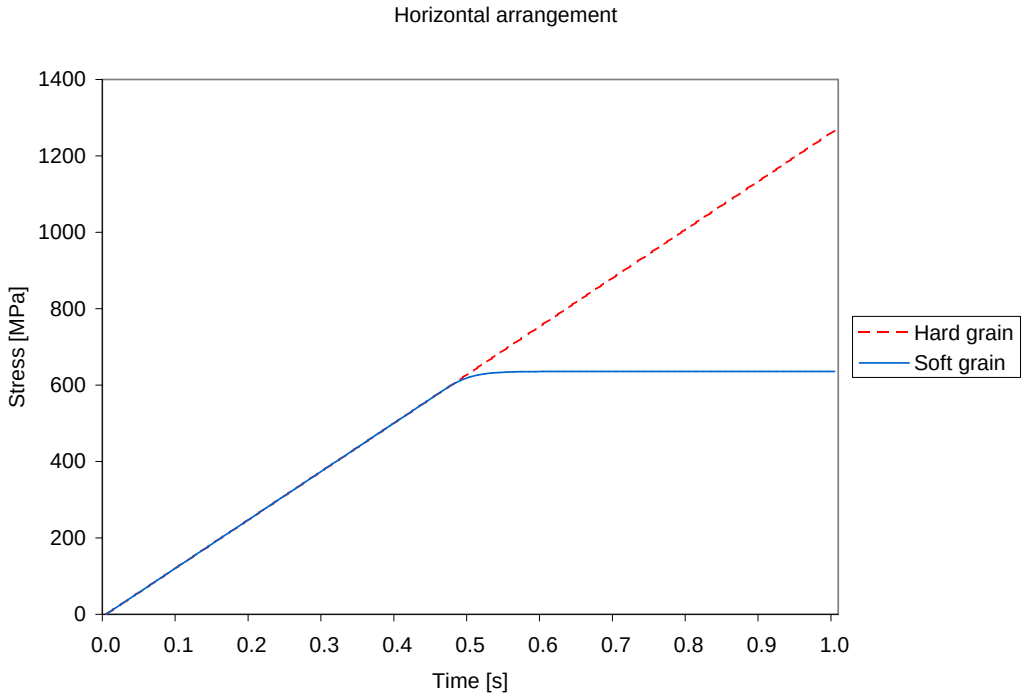

Figure 3.2: Verification of the code: Stress evolution in hard and soft grains in horizontal arrangement.

In order to satisfy force equilibrium, both blocks support the same stress at all times. During the elastic period, the deformation is identical at all points regardless of the orientation of the lattice. However, when the soft grain yields, the stress level is maintained constant, impeding further deformation of the hard grain, hence the strain rate is doubled in the soft one. This behaviour is observed in the test, shown in Figure 3.4, indicating that the code is correctly implemented and the performance of the subroutines is appropriate.

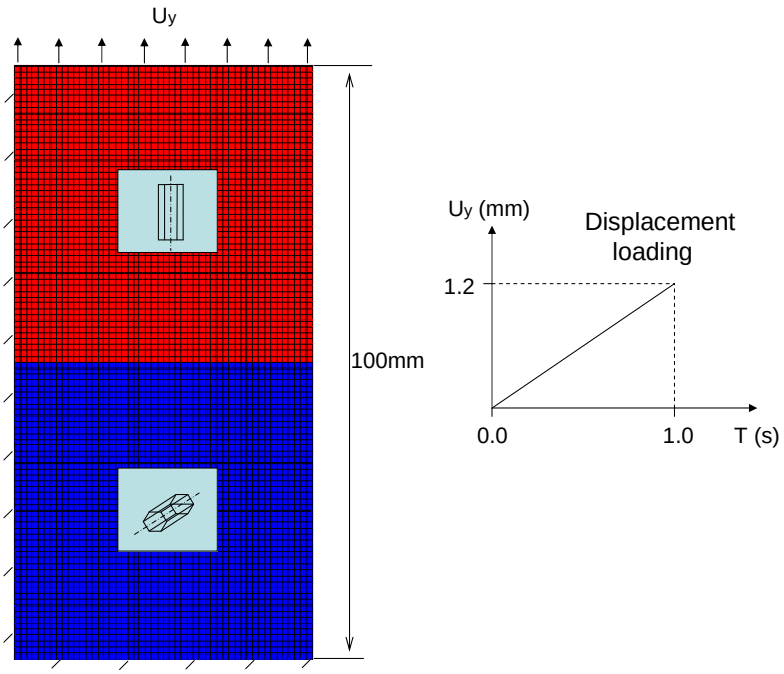

Figure 3.3: Verification of the code: hard and soft grains in vertical arrangement.

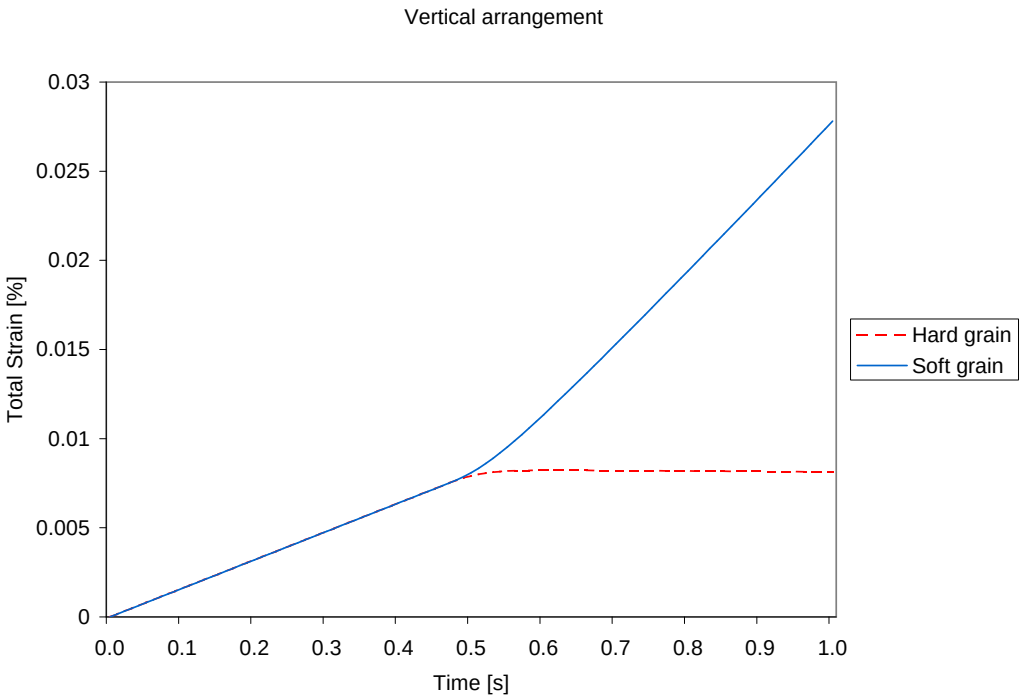

Figure 3.4: Verification of the code: Strain evolution in hard and soft grains in vertical arrangement.

Chapter 4

Crystallography and lengthscale effects in polycrystal deformation

This section presents a simulation on Rolls-Royce production processes for Ti-6Al plates. The effects of crystallographic orientation, the lengthscale and their interaction are investigated at micro- and macro-levels.

A total of four combinations of crystallographic orientations are included in this analysis, each of them simulating a particular manufacturing procedure. In addition, the model is scaled by various factors to provide the necessary data to understand the lengthscale effects, intrinsically induced in the crystal plasticity model.

4.1 Macro-scale crystallography effects

Variations in manufacturing processes lead to differences in the crystal structure of the final material. In consequence, the production procedures have

a strong influence in the macroscopic mechanical behaviour of finished components. These effects are satisfactorily described by the crystal plasticity model under study, in which the crystallographic orientation is a crucial parameter taken into account. In addition, its implementation into the commercial FE package ABAQUS, enables a systematic investigation of such effects.

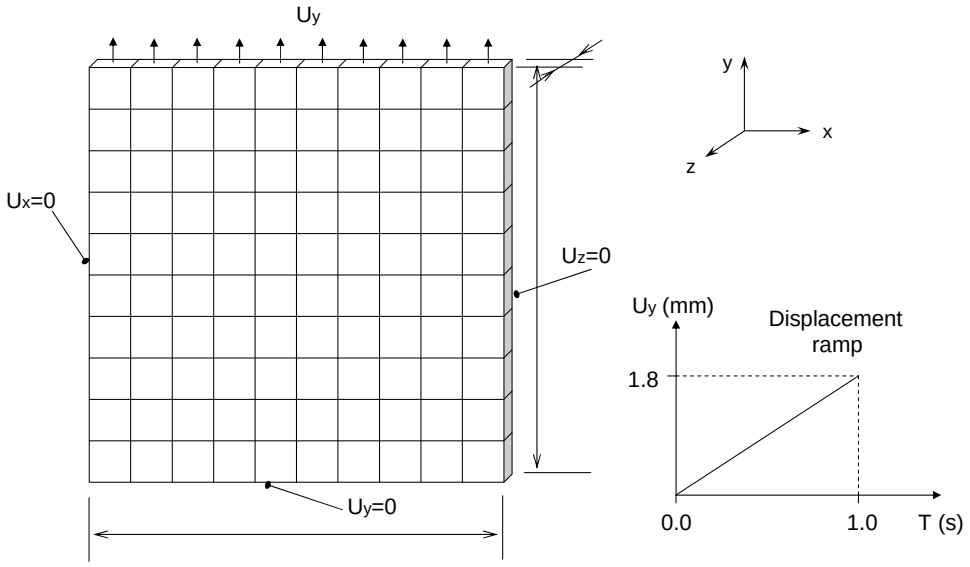

Figure 4.1: Polycrystal model and boundary conditions.

A 3D model of a polycrystal is considered, shown in Figure 4.1. The plate is composed of a hundred grains with 81 elements each, of only one element depth. The boundary conditions are illustrated in Figure 4.1. The bottom, left and back surfaces are constrained in the y-, x- and z-directions respectively. A uniform, ramp-type displacement is applied to the top surface nodes until a 2% macroscopic total strain is reached. The material properties of Ti-

6Al at room temperature are collected in Table 2.2 and the alloy is considered elastically isotropic.

Depending on the manufacturing process being represented, each grain is assigned a particular crystallographic orientation. The four resulting combinations are described next.

- **CASE 1: Unidirectional plate**. The first case represents an unidirectional rolled plate. This procedure causes all the crystals to be orientated towards the rolling direction. For this reason, all grains are relatively soft, regarding the load applied along the y-axis, which is almost perpendicular to the c-axes of the crystals.

  In order to include this structure in the numerical model, the reference configuration shown in Figure 2.1 is rotated 90° about the y-axis. In addition, a random rotation of $\pm 10°$ is applied around the z-axis. In this way, the c-axes of all grains are contained in the xy-plane.

- **CASE 2: Crossed rolled**. In this case, a bidirectional rolling is applied with perpendicular axes. This forces approximately half of the grains to lean towards each rolling direction. When the load is applied, parallel to the y-axis, half the crystals are soft, hence undergo plastic slip, while the other half are stiff and likely to remain elastic under such conditions.

  The distribution of the c-axes assigned to each grain is again modified. Half of the units undergo a 90° rotation about the x-axis, while the other half rotate a similar angle around the y-axis. Once again, a random rotation of $\pm 10°$ about the z-axis is applied to the whole mesh.

- **CASE 3: Blade**. As indicated by its name, this case represents the material employed in blade construction. The c-axes of the unit cells of the crystals are contained in the xy-plane, randomly rotated around the y-axis. This configuration is similar to the first case, regarding the loading conditions of the model. Moreover, the individual grains are softer that those of the unidirectional rolling plate, as they have not suffered any rotation about the z-axis. Nevertheless, the relative

orientation of adjacent crystals and therefore their interactions, vastly differ from one case to another.

In order to introduce this configuration into the code, the unit cell of each grain is randomly rotated about the y-axis, remaining perpendicular to it.

- **CASE 4: Complete random**. A uniform matrix of material with no preferred configuration is considered last. The crystals are randomly orientated throughout the plate, hence both hard and soft grains may be contained in the sample.

The macro-scale stress-strain response to constant strain rate monotonic loading is represented in Figure 4.2. The macro-scale stress is obtained as the average stress of the top elements, which in turn, is the mean of the stresses at their integration points. The macro-scale strain is simply obtained from the change of length of the overall model. Under the assumption of isotropic elasticity, the elastic period of the curves is not altered by the orientation rearrangement. These modifications only affect the plastic behaviour.

It is worth noticicing that crystallography introduces hardening in two ways. The former is the due to the fact that polycrystals are able to increase the carried load until all grains in any cross-section become plastic. The latter is caused by the generation of GNDs, whose density grows with spatial deformation gradients, as explained in Section 2.2.2. The hardening introduced by the SSDs is negligible in this study since the constant h, in equation 2.8, is set equal to the small value of 50 and its density is fixed. Nevertheless, the former process of material hardening also dominates against the GNDs formation.

These phenomena readily explain the significant differences from the four cases considered. The cross-rolled plate arrangement, in which approximately half of the material is unfavourable to slip, gives rise to the highest hardening. By the same token, the randomly distributed configuration shows appreciable hardening, since it contains a wide range of orientations, whose ease to slip differs from each other. However, the slope of the curves corresponding to

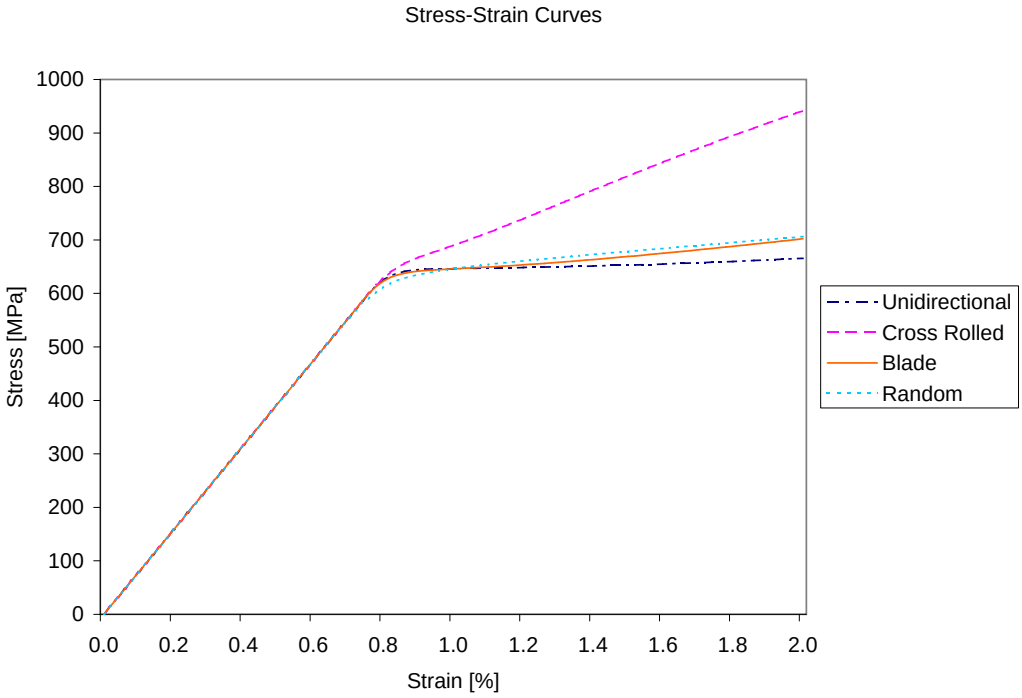

Figure 4.2: Orientation effects in macro-scale stress-strain responses under constant strain rate.

the first and third cases, whose grains are more uniformly distributed, are comparatively small, being higher in the latter due to higher deformation gradients.

4.2 Macro-scale lengthscale effects

Most standard constitutive models for the mechanical behaviour of solids used in engineering applications consider that the stress at a given point uniquely depends on the values of deformation at that point only. These

local theories rely on the assumption that the material can be treated as a continuum at an arbitrarily small scale, shown to be adequate if the characteristic wave length of the deformation field remains above the resolution level of the material model [Bažant and Jirásek, 2002]. No length scale parameter is therefore present in the constitutive equations of these scale independent models.

Conversely, below the resolution level, the model needs to be enriched so as to capture the strong size-dependence that materials are experimentally shown to exhibit [Shu and Fleck, 1999]. The well known Hall-Petch phenomenon is an example of length effect. The physical reasoning behind the Hall-Petch law is the accumulation of dislocations at the grain boundaries. The stress necessary to push the dislocations into the next grain diminishes as dislocations pile up.

Scale dependence is intrinsically introduced into the crystal plasticity model under study in this work, by means of a gradient-type non local model. Size-dependent plasticity is based on geometrically necessary dislocations (GNDs), whose density evolves proportional to the derivatives of the plastic strain field, (Eq. 2.6, Section 2.2.2).

The lengthscale effects in the macro-scale response of the polycrystal are subsequently investigated. The model shown in Figure 4.1 is adopted again here with overall dimensions scaled by factors of 1, 5, 10 and 100. Crystallographic configuration and grain morphology are not modified. A identical polycrystal is therefore analysed with varying lengths of 90, 450, 900 and 9000 μm, corresponding to grain sizes of 1, 5, 10 and 100 μm.

The macro-scale stress-strain response to constant strain rate, monotonic loading is represented in Figure 4.3. The macro-scale stress and strain are obtained following the procedure explained in Section 4.1. The density of GNDs is now the controlling factor which determines the amount of hardening the material develops. The mismatch of slip bands at the grain boundaries or the presence of hard, non deforming particles generate gradients of plastic strain which enlarge the density of GNDs, leading to hardening. As

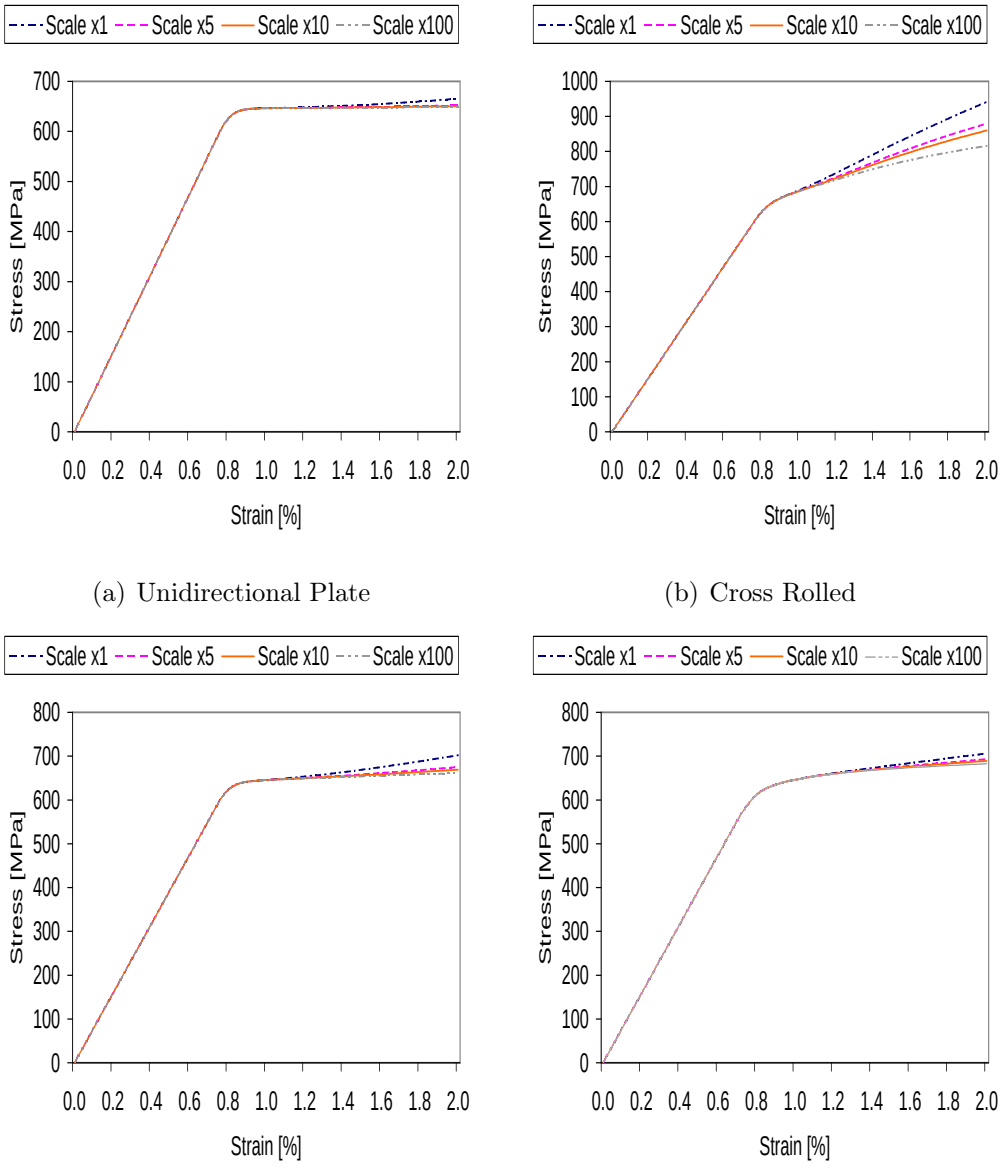

(a) Unidirectional Plate

(b) Cross Rolled

(c) Blade

(d) Random

Figure 4.3: Lengthscale effects in macro-scale stress-strain responses under constant strain rate.

grain size decreases, larger gradients are developed, hence higher slopes in the plastic period of the stress-strain curves are observed.

However, this effect is naturally less pronounced in cases 1 and 3, whose more uniform configuration hinders the development of high plastic strain gradients, regardless of the grain size.

4.3 Effects interaction in slip accumulation

Plastic slip accumulation is thought to play an important role in polycrystals failure process [Dunne et al., 2007c] and it is discussed in the following section. It is therefore interesting to analyse the influence of crystallography orientation and lengthscale in the slip distribution.

The information needed for the study is taken from the 16 FE analyses corresponding to the four cases in Section 4.1, scaled by factors of 1, 5, 10 and 100. The accumulated plastic strain range, that is, the difference between the maximum and the minimum accumulated plastic strain at all integration points, is calculated and plotted in Figure 4.4, against the lengthscale factor. Four curves corresponding to the four cases are thus obtained. It may be seen that the heterogeneity of the structure causes higher accumulation of plastic deformation in certain grains while others may even remain elastic. In the cases with a more uniform crystallographic combinations, the slip is more equally distributed over the entire model.

The lengthscale also affects the predicted slip fields. As grain size increases, lower gradients are developed, that is, lower hardening, which results in higher accumulation of plastic strains, Figure 4.4.

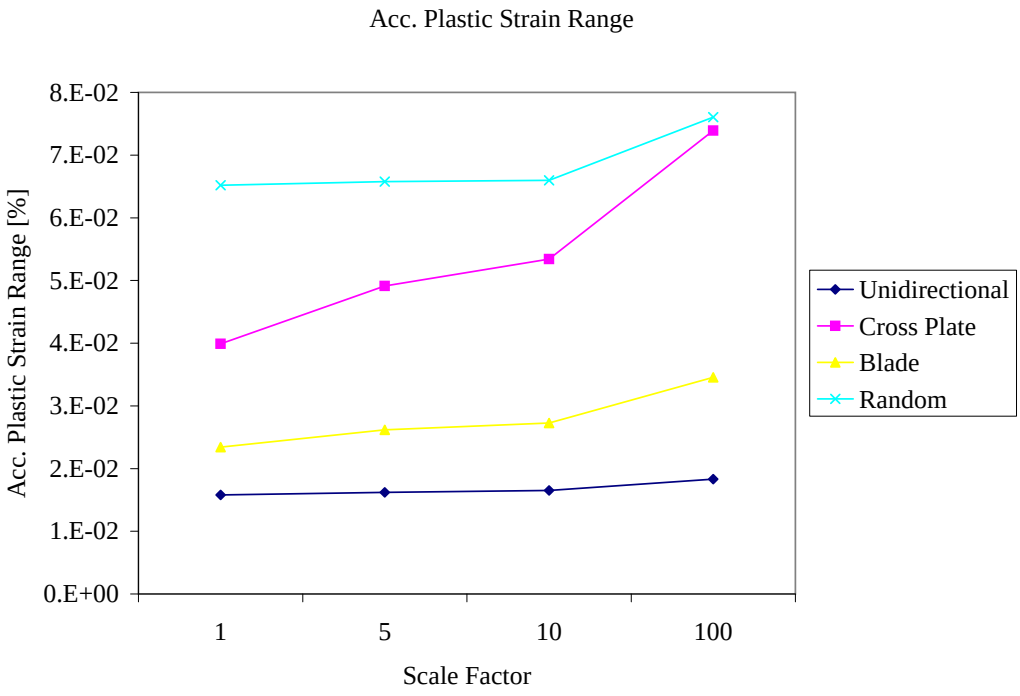

Figure 4.4: Orientation and lengthscale effects interaction in slip accumulation.

Chapter 5

Monotonic failure in hcp crystals

A wide range of titanium alloy components are affected by the phenomenon of *faceting*, or, micro-crack development at about the length of the grain size, almost always associated with an hcp basal plane. If faceting occurs at a large grain, where grain is understood as a region of approximately uniform crystallographic orientation, the subsequent propagation time of the crack to an unacceptable length may be limited.

5.1 Faceting formation

A systematic study performed by Dunne et al. [2007b], shows that the combinations of crystallographic orientations in neighbouring grains influence the local stress and accumulated slip distribution. The configuration termed as *rogue grain*, revealed as the most unfavourable, is that in which a hard grain with c-axis near-parallel to the loading direction, is adjacent to softer grains, with c-axis near-normal to the loading direction and a prismatic slip plane at approximately 70° to the normal to the load, Figure 5.1. This particu-

lar combination leads to the highest stress normal to the hard grain basal, together with the highest level of accumulated plastic strain in the adjacent soft grains. However, crystallography alone cannot explain some features associated with faceting, such as volume dependence.

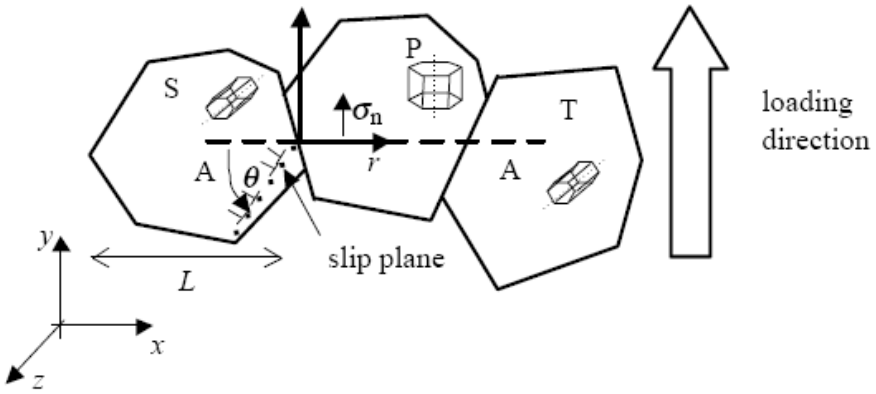

Figure 5.1: Schematic of a rogue grain combination. A typical set of prismatic slip planes is represented in grain S, oriented at an angle θ to the x-axis. $\theta = 70°$ is shown the most unfavourable angle. [Dunne et al., 2007b]

Moreover, the morphology-crystallography interaction is found to be of importance, since it may lead to a localized accumulation of slip in the soft grain combined with a significant penetration of plastic slip into the adjacent hard grain. The range of grain boundary angle over which this occurs is rather narrow, namely within $\pm 5°$ off the angle at which the orientations of the boundary and the active prismatic slip plane coincide.

Cold dwell also plays an important role in faceting. Under conditions of load control, a hold results in *load shedding*, that is, stress relaxation in the softer material due to creep straining, which leads to increasing stress in the hard grain. Conversely, a strain hold under strain control loading, results in stress relaxation in the hard grain, accompanied by further accumulation of plastic slip in the softer material. Nevertheless, it is important to notice that the hold itself does not contribute to faceting, however, during the hold, the rate dependence of the Ti alloy leads to either load shedding under a load hold, or plastic strain accumulation under a strain hold.

Recapitulating these ideas, the formation of facets requires:

- the existence of a rogue grain combination,
- the boundary between the hard and the soft grain having a morphological orientation coincident with a crystallographically active slip plane in the soft grain, and
- a loading cycle such that load shedding or stress relaxation may lead to increased accumulated slip.

Further details on the effects of morphology and crystallography in hcp crystals may be found in Dunne et al. [2007b], whose main conclusion is quoted here:

> *We therefore hypothesize that it is the localized penetration of slip into the hard grain which, under conditions of cyclic loading, results in the generation of a persistent slip band and subgrain-level microcrack generation. Under the action of the high basal stresses, normal to the grain c-axis, which exist in the circumstances outlined, the nucleated defect propagates through the grain, parallel to the basal plane, until it hits the boundaries of the adjacent softer grains.*

5.2 Failure in the presence of a rogue grain combination

The potential damage of a hard grain embedded in a matrix of soft material, causing high stress and accumulated plastic slip local to the boundary, leads to the thought that, under monotonic loading conditions, the presence of a rogue grain is likely to control the failure of the material as well. Thus, a criterion is proposed under this assumption and applied to a FEM modelled polycrystal. The results and conclusions are provided in this section.

5.2.1 Nucleation criterion

Faceting is more frequently observed under load control than under strain control. Given this, and the previous considerations on load shedding and strain control dwell, facet formation is considered a stress-controlled process and a nucleation criterion is proposed based on the stress normal to the basal plane. When a critical stress normal to the basal plane is reached, the material fails and a crack is nucleated.

In order to incorporate the failure criterion into the crystal plasticity constitutive equations, elastic-damage coupling is included reducing the material stiffness by a factor of $1-\omega$, so that $\boldsymbol{D} = \boldsymbol{D}_0(1-\omega)$.

The damage also affects the plastic formulation such that the stress is now defined as

$$\boldsymbol{\sigma} = \boldsymbol{D}\boldsymbol{\varepsilon}^{\mathrm{e}} = \boldsymbol{D}_0(1-\omega)\left(\boldsymbol{\varepsilon}^{\mathrm{e}}_{(\mathrm{t})} + \Delta\boldsymbol{\varepsilon}^{\mathrm{e}}\right) = \boldsymbol{\sigma}^{\mathrm{tr}}(1-\omega) - \boldsymbol{D}_0(1-\omega)\Delta\boldsymbol{\varepsilon}^{\mathrm{p}},$$

which gives the residual equation

$$\boldsymbol{\Psi} = \boldsymbol{\sigma} - \boldsymbol{\sigma}^{\mathrm{tr}}(1-\omega) + \boldsymbol{D}_0(1-\omega)\Delta\boldsymbol{\varepsilon}^{\mathrm{p}} = \boldsymbol{0}.$$

Recalling that $\delta\Delta\boldsymbol{\varepsilon}^{\mathrm{p}} = \boldsymbol{P}\delta\boldsymbol{\sigma}$, Newton algorithm scheme states that

$$\boldsymbol{\Psi} + \frac{\partial \boldsymbol{\Psi}}{\partial \boldsymbol{\sigma}}\delta\boldsymbol{\sigma} = [\boldsymbol{\sigma} - \boldsymbol{\sigma}^{\mathrm{tr}}(1-\omega) + \boldsymbol{D}_0(1-\omega)\Delta\boldsymbol{\varepsilon}^{\mathrm{p}}] + [\boldsymbol{I} + \boldsymbol{D}_0(1-\omega)\boldsymbol{P}]\delta\boldsymbol{\sigma} = \boldsymbol{0},$$

so the stress can now be updated iteratively by

$$\delta\boldsymbol{\sigma} = [\boldsymbol{I} + \boldsymbol{D}_0(1-\omega)\boldsymbol{P}]^{-1}\left\{\boldsymbol{\sigma} - \boldsymbol{\sigma}^{\mathrm{tr}}(1-\omega) + \boldsymbol{D}_0(1-\omega)\Delta\boldsymbol{\varepsilon}^{\mathrm{p}}\right\}.$$

The consistent elastic-plastic stiffness matrix is also modified in the same way as the trial stress. Starting from the stress definition

$$\delta\boldsymbol{\sigma} = \delta\boldsymbol{\sigma}^{\mathrm{tr}} + \boldsymbol{D}\delta\Delta\boldsymbol{\varepsilon}^{\mathrm{p}},$$

introducing the trial stress differential

$$\delta\boldsymbol{\sigma}^{\mathrm{tr}} = \delta\left[\boldsymbol{D}_0(1-\omega)\left(\boldsymbol{\varepsilon}^{\mathrm{e}}_{(t)} + \Delta\boldsymbol{\varepsilon}\right)\right] \equiv \boldsymbol{D}_0(1-\omega)\delta\boldsymbol{\varepsilon},$$

and the plastic strain increment differential $\delta\Delta\boldsymbol{\varepsilon}^{\mathrm{p}} = \boldsymbol{P}\delta\boldsymbol{\sigma}$, results in

$$\delta\boldsymbol{\sigma} = \boldsymbol{D}_0(1-\omega)\delta\boldsymbol{\varepsilon} - \boldsymbol{D}_0(1-\omega)\boldsymbol{P}\delta\boldsymbol{\sigma},$$

so the Jacobian is finally given by

$$\boldsymbol{C}^{\mathrm{ep}} = \frac{\partial\boldsymbol{\sigma}}{\partial\boldsymbol{\varepsilon}} = [\boldsymbol{I} + \boldsymbol{D_0}(1-\omega)\boldsymbol{P}]^{-1}\boldsymbol{D}_0(1-\omega). \tag{5.1}$$

Nevertheless, in order to represent the nucleation of an actual crack, ω should be close to unity. However, such a high value gives rise to severe convergence problems after the crack formation. Aiming a tentative growth analysis, ω is set to 0.75 to avoid numerical instabilities.

5.2.2 FEM simulation

Simulations are carried out on the polycrystal model earlier employed by Dunne et al. [2007a], adopted here to further research on failure. The 2D

plain strain polycrystal, shown in Figure 5.2, comprises 27 grains of an average size of 20 μm. The grain morphology is arbitrarily specified to represent the true microstructure. A rogue grain combination, marked out in bold lines, is included with the c-axis parallel to the loading direction. Nevertheless, despite its orientation, the hard grain may still undergo limited slip, since the stress field is modified at the local level. The adjacent grains are assigned prismatic slip planes forming angles of about 70° to the primary grain basal plane. All other grains are randomly orientated within ±10° off the reference configuration in Figure 2.1. The bottom and left surfaces are constrained in the y- and x-directions respectively. The top surface is constrained to remain straight. A two seconds ramp load is applied to a top node, and then held for a similar amount of time. The critical stress normal to the basal plane is set to 1150 MPa. Elastic anisotropy is assumed.

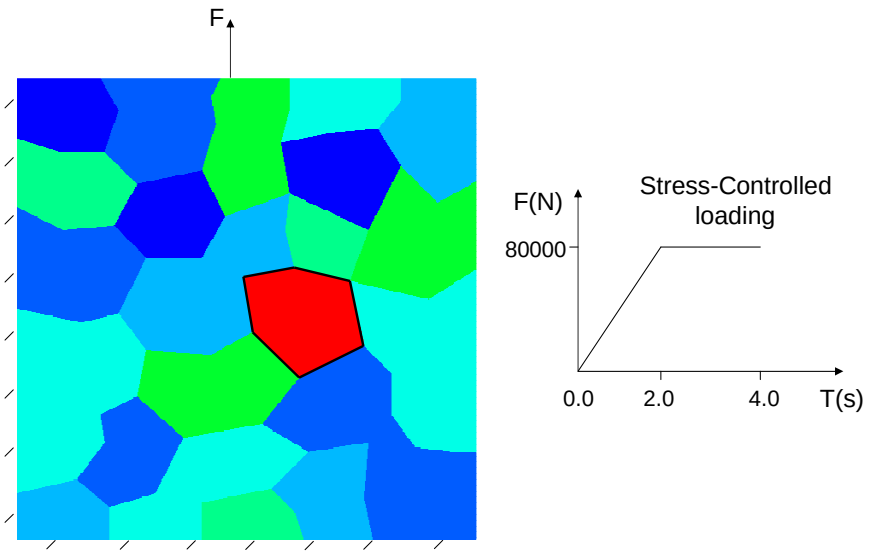

Figure 5.2: Model of a polycrystal containing a rogue grain marked out in bold lines.

The results of the simulation are illustrated in Figures 5.3 and 5.4. As expected, the sample first fails within the hard grain, which still remains elastic, next to the boundary with the soft crystal, whose plastic slip accumulation is highest. After only a few steps, failure is distributed over most of the hard grain. However, in despite of the goodness of the nucleation, the predicted stress distribution is physically meaningless, since the failed crystal is still carrying the highest stress.

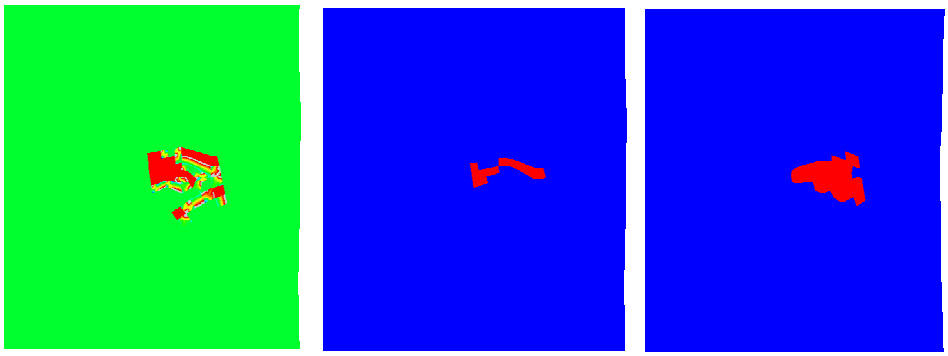

Figure 5.3: Failure in the presence of a rogue grain for various formulations: a) Damage at integration points at t=4 s. b) Damage as an element variable at t=4 s. c) Progressive damage as an element variable at t=4 s.

This unexpected result may be explained by the fact that failure is implemented at the integration points, based solely on the state of that particular point. This local formulation together with the redistribution of forces in

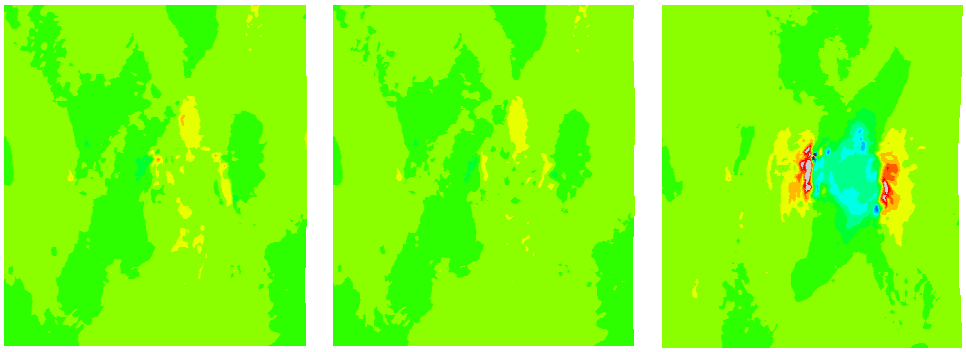

Figure 5.4: Stress field in the loading direction, σ_{yy}, in the presence of a rogue grain for various formulations: a) Damage at integration points at t=4 s. b) Damage as an element variable at t=4 s. c) Progressive damage as an element variable at t=4 s.

the vicinity of the damaged points, permit some integration points to remain unfailed and therefore support considerable amounts of load.

In order to avoid unlocalised damage, the criterion is modified to account for the influence of neighbouring points in the fracture process. Thus, damage is dealt with as an element variable. When the average stress at the element reaches the critical value, the whole element loses its stiffness.

The new approach improves the localization of the damage. Elements fail following a defined path, Figure 5.3. The estimated crack starts at the spot

mentioned earlier and propagates through the grain, parallel to the basal plane. Another crack nucleates after a short time, local to the left hard-soft boundary and propagates through the hard grain in opposite direction, until it merges with the former crack. However, the hard grain still supports elevated levels of stress.

Therefore, a new modification is made to improve the formulation. In order to prevent the material from carrying any load once failed, it is necessary to further diminish the stiffness of the material. With the aim of avoiding convergence problems, the reduction is applied over several steps. When the average stress at the element reaches the critical value, its stiffness becomes 65% smaller and continues dicreasing in following steps as

$$D_{(n)} = (1 - \omega)D_0,$$

where

$$\omega = 0.65 + 0.035\Delta t,$$

up to $\omega = 0.95$.

The progressive stiffness reduction may be understood as the progressive loss of stiffness as the crack propagates through the element at a constant rate. However, the lack of experimental data together with the strong mesh dependence impede the adjustment of the growth rate.

These modifications considerably improve the results. Failed elements are successfully prevented from carrying significant load, which is progressively redistributed towards the undamaged material. The results of the three analyses are compared in Figures 5.3 and 5.4. It is important to notice that the wider damaged area within the last approach in Figure 5.3, corresponds to approximately the same number of elements as that within the second formulation, which undergo much larger deformations due to a larger reduction of stiffness. These results are therefore closer to the experimentally expected behaviour.

Furthermore, if the load is augmented up to 90000 MPa, the crack eventually overcomes the grain boundary barriers at the end of the hold period,

propagating through the adjacent grains, Figure 5.5.

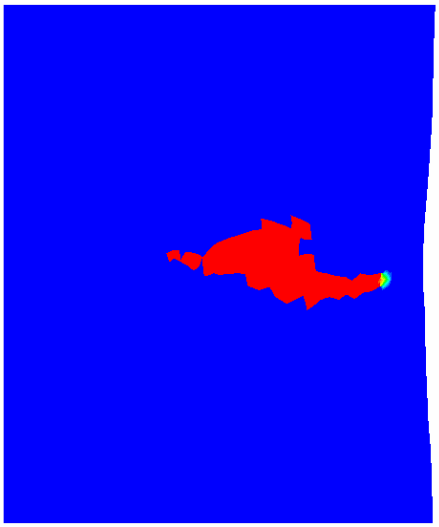

Figure 5.5: Under a higher load, the crack overcomes the barriers and propagates.

In conclusion, a failure criterion is proposed and simulated based on the stress normal to the basal plane. When this stress reaches a critical value, the stiffness of the material is reduced by several methods, at both integration point and element levels. The implementation of damage as an element variable seems to provide better results. Under these conditions, it is shown that failure occurs within the rogue grain. The most striking feature is the nucleation of the crack in the hard grain, local to the grain boundary where the maximum accumulated plastic slip is predicted. This may confirm the influence of such parameter in the process. The crack continues growing throughout the hard grain until it reaches the next boundary. It is worth indicating that plastic slip still accumulates during the load hold and that part of the crack growth occurs during that period.

5.3 Failure in the absence of rogue grain combinations

In the absence of rogue grain combinations, the fracture criterion developed in the previous section is no longer appropriate to predict crack nucleation. In a piece of material with all grains favourably orientated to slip, the stress normal to the basal plane is maintained at moderate levels due to plastic slip. Therefore, a new criterion is necessary to include these circumstances.

5.3.1 Nucleation criterion

Experimental results are available from a sample of soft material tested at Swansea University [Bache, 2007]. Stress control tensile test with load dwell was carried out on the sample, which exhibits fracture perpendicular to the loading direction, as shown in Figure 5.7. This leads to the development of the view that the stress parallel to the loading direction controls the process. When it reaches a certain value, the material fails and its stiffness is reduced by a factor of $1 - \omega$, where $\omega = 0.75$, so that $\boldsymbol{D} = \boldsymbol{D}_0(1 - \omega)$. The implicit integration equations are again modified as described in Section 5.2.1.

The same three approaches developed earlier are now applied following the same steps, with the only difference at element level, (approaches b) and c) in Figures 5.3, 5.4, 5.8 and 5.8). Failure occurs when the first integration point reaches the critical stress, as opposed to the averaged value used before.

5.3.2 FEM simulation

A 2D plain strain polycrystal model is used to reproduce the conditions of the experiment. Grain morphology and orientation were determined by Bache

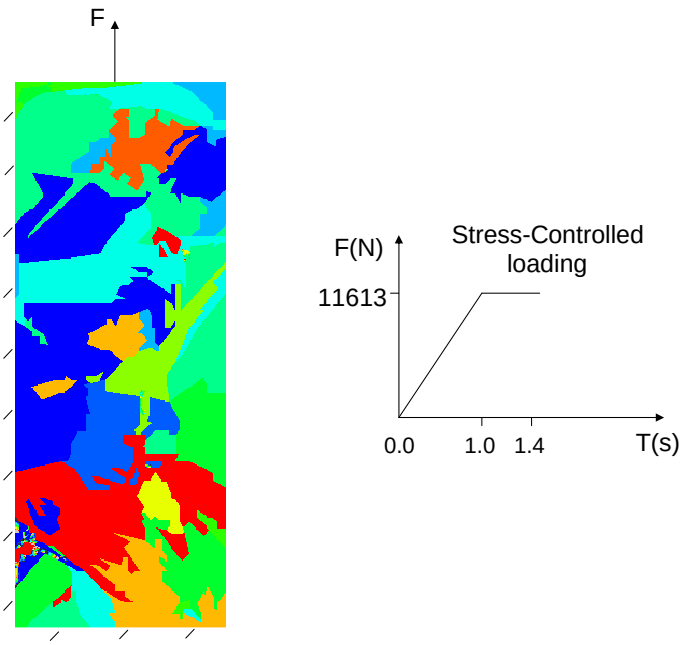

Figure 5.6: Polycrystal model of the experimental sample.

[2007] using electron back scatter diffraction (EBSD), indicated by differing colours in Figure 5.6. The bottom and left surfaces are constrained in the y- and x-directions respectively. The top surface is constricted to remain straight. A one second ramp load is applied to a top node, and then held for 400 milliseconds. The critical stress parallel to the loading direction is set to 750 MPa. Elastic anisotropy is assumed.

Three analyses are performed under the approaches described in the previous section. The results are shown in Figure 5.7 and 5.8. In the three studies, a crack initiates approximately at the centre of the specimen, which coincides with the experimental evidence. However, further growth is only adequately represented by the failure model implemented at the element level, that is, the whole element loses its stiffness when the average stress reaches the critical

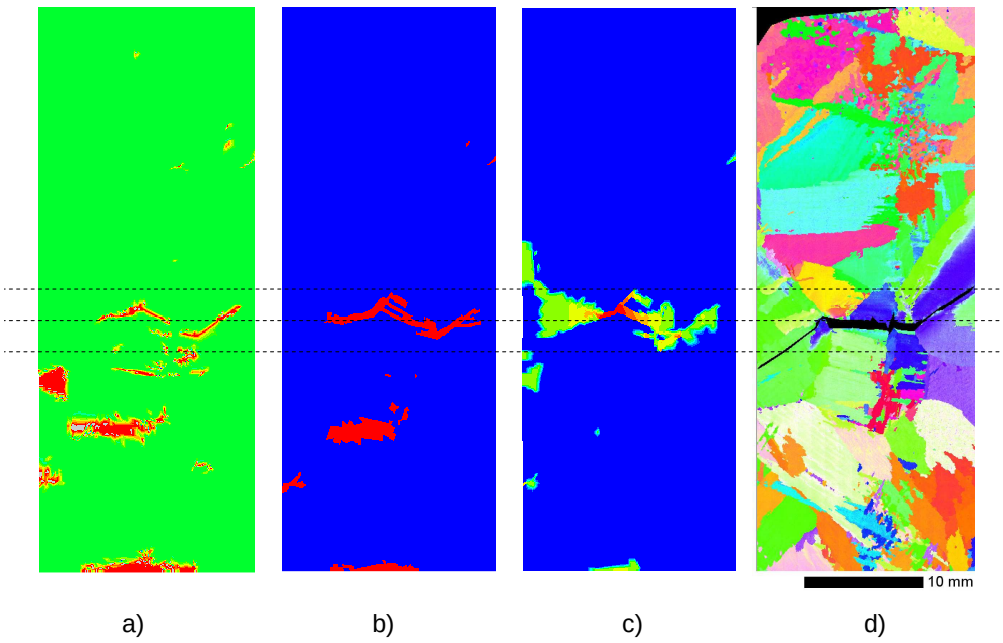

Figure 5.7: Failure in the Swansea sample for various formulations: a) Damage at integration points at t=0.96 s. b) Damage as an element variable at t=0.90 s. c) Progressive damage as an element variable at t=0.88 s. d) Experimental fracture.

value. In addition, it seems to be better reproduced by the single reduction step criterion. It may be readily explained by the uniform stress field across the section, probably leading to very high growth rate. The predicted crack follows a path similar to that in the sample test until the analysis stops due to convergence problems. The strain field obtained from the element approach is also comparable to that in the experiment specimen, Figure 5.8.

Therefore, it may be concluded that a failure criterion based on the stress parallel to the loading direction, in which the stiffness of an element is reduced up to 75% when the stress at any of its integration points reaches a critical

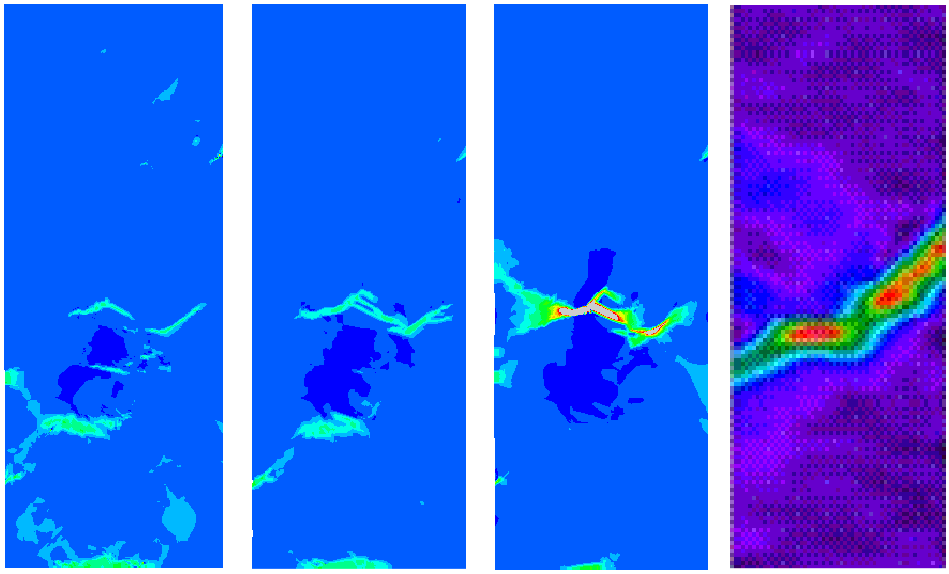

Figure 5.8: Total strain field in the loading direction, ε_{yy}, in the Swansea sample for various formulations: a) Damage at integration points at t=0.96 s. b) Damage as an element variable at t=0.90 s. c) Progressive damage as an element variable at t=0.88 s. d) Experimental deformation.

value, successfully predicts the crack nucleation, and qualitatively describes the directions of subsequent growth.

5.4 Elastic anisotropy effects in failure

Dunne et al. [2007a] show that, at the macro-scale, the effect of elastic anisotropy is rather insignificant compared to that of anisotropic plasticity,

caused by slip of differently orientated grains. However, at grain level, it may lead to noticeable differences in accumulated plastic slip, which is considered of significance in crack nucleation.

Elastic anisotropy effects in crack nucleation and growth are investigated. Isotropic elasticity is introduced in the two models by simply assuming the z-direction modulus equal to that in the two orthogonal directions.

The three previous studies are performed firstly on the rogue-grain polycrystal of Figure 5.2. The isotropic condition does not significantly affect the nucleation and subsequent growth process. The crack initiates a few seconds earlier at the same location, due to the large plastic strain developed, and propagates as described above.

However, the simulations on the Swansea sample in Figure 5.6 surprisingly bring into light a strong dependence on the elastic behaviour. It may be seen in Figure 5.9, that the strain fields under the elastic isotropy assumption differs vastly from the others. It provokes the material to fail in the bottom of the sample, far from the anisotropic and the experimental results.

A possible explanation may lay in the homogeneous or otherwise structure of the model. It may be possible that elastic anisotropy becomes important as plastic anisotropy diminishes. This explains the absence of effects in the former model, strongly plastically anisotropic, as well as the differences encountered in the latter, with more homogeneous crystallography.

It is concluded, therefore, that the assumption of the elastic behaviour needs to be considered carefully, since it may noticeably influence the results of any simulation.

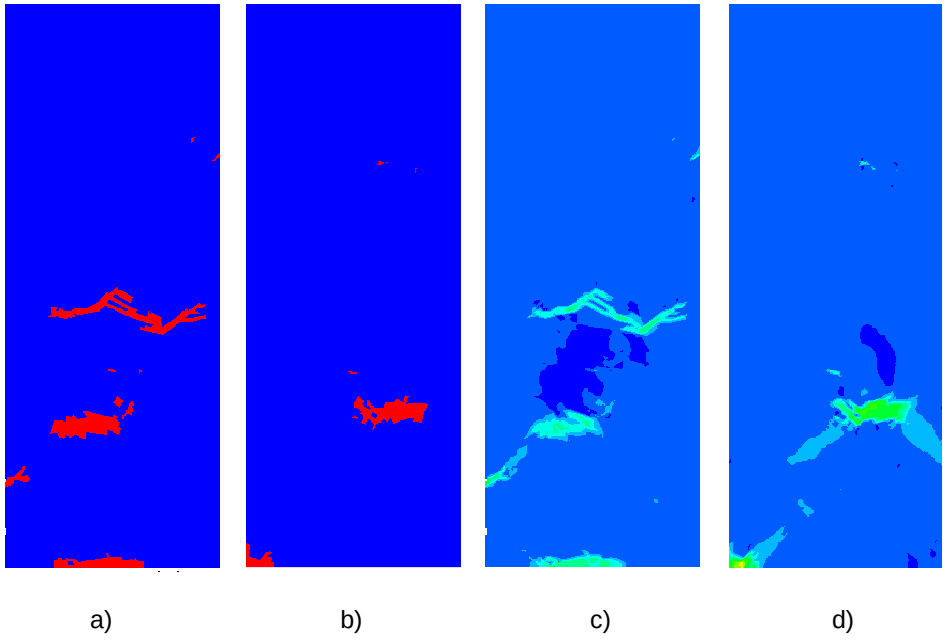

Figure 5.9: Isotropic and anisotropic failure and strain fields for damage at element element. a) Elastically anisotropic failure. b) Elastically isotropic failure. c) Elastically anisotropic strain field. d) Elastically isotropic strain field.

Chapter 6

Conclusions and Further work

Implicit integration of crystal plasticity has been implemented into ABAQUS and verified by means of a simple two grains model. Crystallographic microstructure has been shown to have significant influence in the macro- and micro-scale response of the material. Hardening caused by unfavourably orientated grains has been found considerably higher than that due to plastic strain gradients generated by orientation mismatch.

Lengthscale effects have been successfully represented by the intrinsic size-dependence introduced by the density of geometrically necessary dislocations. It has been demonstrated that as size increases, hardening diminishes and further plastic slip accumulates.

Failure under monotonic loading containing a dwell period has been addressed by various criteria and predictions have fitted the experimental data. A failure criterion based on the stress normal to the basal plane has been implemented and nucleation has occurred within the rogue grain, local to the grain boundary where the maximum accumulated plastic strain has developed. This has possibly confirmed the influence of slip accumulation in facet formation. Further research should clarify the role of plastic slip and

determine the appropriate way of including, if necessary, this parameter into the damage criterion.

In the absence of rogue grain combinations, a failure criterion based on the stress parallel to the loading direction has successfully predicted the nucleation, and qualitatively described the directions of subsequent growth of a crack observed in the experimental sample being simulated.

Moreover, some polycrystals have been reported to exhibit a strong dependence on the elastic behaviour. Vast differences in strain fields and consequent crack formation have arisen depending on the assumptions made concerning isotropy or anisotropy.

On the other hand, major problems of convergence and mesh-dependence would be avoided with the assessment of a non-local approach in modelling failure. This should therefore be the next step to follow in this line of research.

In summary, various studies have been carried out on the titanium alloy Ti-6Al, bringing into light several interesting features. Experimental data is now a prime requirement in order to validate these observations and reinforce the conclusions.

Bibliography

M.R. Bache. Internal report. university of wales, swansea. 2007.

M.R. Bache. A review of dwell sensitive fatigue in titanium alloys: the role of microstructure, texture and operating conditions. *International Journal of Fatigue*, 25:1079–1087, 2003.

M.R. Bache, M. Cope, H.M Davies, W.J. Evans, and G. Harrison. Dwell sensitive fatigue in a near alpha alloy at ambient temperature. *International Journal of Fatigue*, 19:83–88, 1997.

Z.P. Bažant and M. Jirásek. Nonlocal integral formulations of plasticity and damage: Survey of progress. *Journal of Engineering Mechanics-ASCE*, 128:1119–1149, 2002.

E.P. Busso, F.T. Meissonnier, and N.P. O'Dowd. Gradient-dependent deformation of two-phase single crystals. *Journal of the Mechanics and Physics of Solids*, 48:2333Ű2361, 2000.

A.H. Cottrell. Theory of dislocations. *Progress in Metal Physics*, 1:77–&, 1949.

A.M. Cuitiño and M. Ortiz. Computational modelling of single crystals. *Modelling and Simulation in Materials Science and Engineering*, April 1993.

F.P.E. Dunne and N. Petrinic. *Introduction to Computational Plasticity*. Oxford University Press, 2005.

F.P.E. Dunne, D. Rugg, and A. Walker. Lengthscale-dependent, elastically anisotropic, physically-based hcp crystal plasticity: Application to cold-

dwell fatigue in Ti alloys. *International Journal of Plasticity*, 23:1061–1083, 2007a.

F.P.E. Dunne, A. Walker, and D. Rugg. A systematic study of hcp crystal orientation and morphology effects in polycrystal deformation and fatigue. *Proceedings of The Royal Society A-Mathematical Physical and Engineering Sciences*, 463:1364–5021, 2007b.

F.P.E. Dunne, A.J. Wilkinson, and R. Allen. Experimental and computational studies of low cycle fatigue crack nucleation in a polycrystal. *International Journal of Plasticity*, 23:273–295, 2007c.

R.T. Fenner. *Finite Element Methods for Engineers*. The MacMillan Press Ltd, 1975.

N.A. Fleck, G.M. Muller, M.F. Ashby, and J.W. Hutchinson. Strain gradient plasticity: Theory and experiment. *Acta Metallurgica et Materialia*, 42: 475–487, 1994.

H. Gao and Y. Huang. Geometrically necessary dislocations and size-dependent plasticity. *Scripta Materialia*, 48:113–118, 2003.

V. Hasija, S. Ghosh, M.J. Mills, and D.S. Josheph. Deformation and creep modeling in polycrystalline ti-6al. *Acta Mater*, 51:4533–4549, 2003.

S.N. Kuchnicki, A.M. Cuitiño, and R.A. Radovitzky. Efficient and robust constitutive integrators for single-crystal plasticity modeling. *International Journal of Plasticity*, 22:1988–2011, 2006.

A. Manonukul and F.P.E. Dunne. High- and low-cycle fatigue crack initiation using polycrystal plasticity. *Proceedings of The Royal Society A-Mathematical Physical and Engineering Sciences*, 460:1881–1903, 2004.

T. Neeraj, D.-H. Hou, G.S. Daehn, and M.J. Mills. Phenomenological and microstructural analysis of room temperature creep in titanium alloys. *Acta Mater*, 48:1225–1238, 2000.

D. Rugg, M. Dixon, and F.P.E. Dunne. Effective structural unit size in titanium alloys. *Journal of Strain Analysis*, 42, 2007.

J.Y Shu and N.A. Fleck. Strain gradient crystal plasticity: size-dependent deformation of bicrystals. *Journal of the Mechanics and Physics of Solids*, 47:297–324, 1999.

S. Suri, T. Neeraj, G.S. Daehn, D.-H. Hou, J.M. Scott, R.W. Hayes, and M.J. Mills. Mechanisms of primary creep in α/β titanium alloys at lower temperatures. *Materials Science and Engineering A*, 234-236:996–999, 1997.

J.C. Williams, R.G. Baggerly, and N.E. Paton. Deformation behavior of hcp Ti-Al alloy single crystals. *Metallurgical and Materials Transactions A*, 33:837–850, March 2002.

O.C. Zienkiewicz. *The Finite Element Method*. McGraw-Hill, 1977.

Appendix A

Resumen del proyecto

A.1 Breve descripción

El presente trabajo se enmarca dentro del proyecto de colaboración entre la renombrada firma Rolls-Royce y el Departamento de Ingeniería de la Universidad de Oxford.

Durante años, ambas entidades han unificado esfuerzos en la investigación de los materiales empleados en la industria aeronáutica. En concreto, las aleaciones de titanio empleadas en discos y álabes de turbinas han sido y son de primordial interés, al presentar comportamientos que se escapan al conocimiento actual.

Este trabajo se centra en uno de estos vacíos: el fenómeno conocido como *faceting*, o aparición de micro-grietas del tamaño aproximado de grano. Este proceso es normalmente asociado con ciertas combinaciones cristalográficas, por lo que es clara la necesidad de un modelo de comportamiento que recoja las carasterísticas de la microestructura, como son las orientaciones de los

distintos granos que conforman la pieza.

Por este motivo, Dunne et al. [2007a] proponen un modelo de plasticidad policristalina, basado en el estancamiento y posterior liberación de dislocaciones deslizantes, estadísticamente acumuladas, (SSDs), de densidad ρ, y ΔF energía de activación. En dicha formulación, el gradiente de velocidad plástica es definido como

$$\boldsymbol{L}^{\mathrm{p}} = \sum_{\kappa} \rho\, b^2 \nu \exp\left(-\frac{\Delta F}{kT}\right) \sinh\left(\frac{(\tau^{\kappa} - \tau_{\mathrm{c}} - r)b^2}{kT\sqrt{\rho + \rho_{\mathrm{G}}}}\right) \boldsymbol{s}^{\kappa} \otimes \boldsymbol{n}^{\kappa}, \tag{A.1}$$

donde ν es la frecuencia en que las dislocaciones intentan saltar las barreras, con o sin éxito; k es la constante de Boltzman; T la temperatura absoluta; τ^{κ} la tensión tangencial en el sistema κ-ésimo; τ_{c} la tensión tangencial crítica y $\boldsymbol{s}^{\kappa}$ y $\boldsymbol{n}^{\kappa}$ los vectores dirección y normal asociados al κ-ésimo sistema de deslizamiento, respectivamente. El volumen de activación es $b^2 l$, donde l es el camino libre medio, $l = 1/\sqrt{\rho + \rho_{\mathrm{G}}}$, y b la magnitud del vector de Burger.

En esta ecuación, ρ_{G} representa la densidad de dislocaciones geométricamente necesarias. La evolución de dichas dislocaciones en el plano κ de normal $\boldsymbol{n}$ es descrita por Busso et al. [2000] como

$$\Delta\boldsymbol{\rho}_{\mathrm{G}}^{\kappa} = \frac{\Delta\gamma^{\kappa}}{b}\mathrm{curl}[\boldsymbol{n}^{\kappa}\boldsymbol{F}^{\mathrm{p}}], \tag{A.2}$$

donde la deformación tangencial, $\Delta\gamma^{\kappa}$, se calcula a través de la Ecuación A.1, teniendo en cuenta que

$$\boldsymbol{L}^{\mathrm{p}} = \sum_{\kappa} \dot{\gamma}^{\kappa} \boldsymbol{s}^{\kappa} \otimes \boldsymbol{n}^{\kappa}.$$

El comienzo de la plastificación viene marcado por la ley de Schmid, esto es, un cristal bajo carga fluye cuando la tensión tangencial en alguno de sus sistemas de deslizamiento alcanza un valor crítico. Asímismo, tiene en cuenta dos tipos de endurecimiento, el producido por el gradiente del campo de deformaciones plásticas y su consecuente producción de GNDs, y el debido a la acumulación de SSDs, que entorpece su propio movimiento.

La implementación del modelo en el programa comercial de Elementos Finitos ABAQUS, se lleva a cabo a través de un "elemento definido por el usuario", desarrollado en una subrutina UEL. La descripción detallada de la integración implícita de las ecuaciones y del algoritmo empleado, puede encontrarse en los Capítulos 2 y 3 de esta memoria.

A continuación se recogen los resultados más relevantes de la investigación. En primer lugar se describen los resultados del estudio sobre la influencia de la orientación cristalográfica en el comportamiento macro- y micro-mecánico. La dependencia de la escala intrínseca del material es posteriormente enfocada, para terminar con la propuesta de varios criterios de fallo y su implementación en modelos policristalinos.

A.2 Estudio cristalográfico

El comportamiento de policristales a nivel macroscópico está definido por la configuración cristalográfica de su estructura. El hecho de que cada grano del material plastifique a un valor distinto de carga, según su posición relativa, provoca que, mientras existan zonas en estado elástico, la tensión requerida para incrementar la deformación aumente. Esto se traduce en una elevada pendiente del tramo plástico de la curva tensión-deformación del material. Una vez que todos los cristales entran en período plástico, el endurecimiendo es debido únicamente a los dos mecanismos mencionados anteriormente, basados en la generación de dislocaciones.

Resulta por tanto evidente, la necesidad de un análisis del comportamiento macro-mecánico de los materiales provenientes de distintos procesos de fabricación, pues posiblemente, las estructuras adquieren ciertas orientaciones preferentes según el procedimiento.

Así, un total de cuatro casos son considerados bajo estudio. Compuestos de la misma aleación pero cuya microestructura se adapta para simular el

proceso de fabricación al que han sido sometido. Dichos prodecimientos y las combinaciones resultantes se detallan en el Capítulo 4. Los resultados se resumen en la Figura A.1.

En dicha gráfica puede observarse un importante endurecimiento en el caso designado como "Cross Rolled", que corresponde a la mayor proporción de material en posición desfavorable para la plastificación, permaneciendo por tanto elástico. Las configuraciones "Unidirectional" y "Blade" muestran una menor pendiente debido a la mayor uniformidad de su microestructura. Es más, la diferencia entre ambas curvas es causada por otro de los tipos de endurecimiento ya mencionados, el debido al gradiente del campo de deformaciones, más pronunciado en este último.

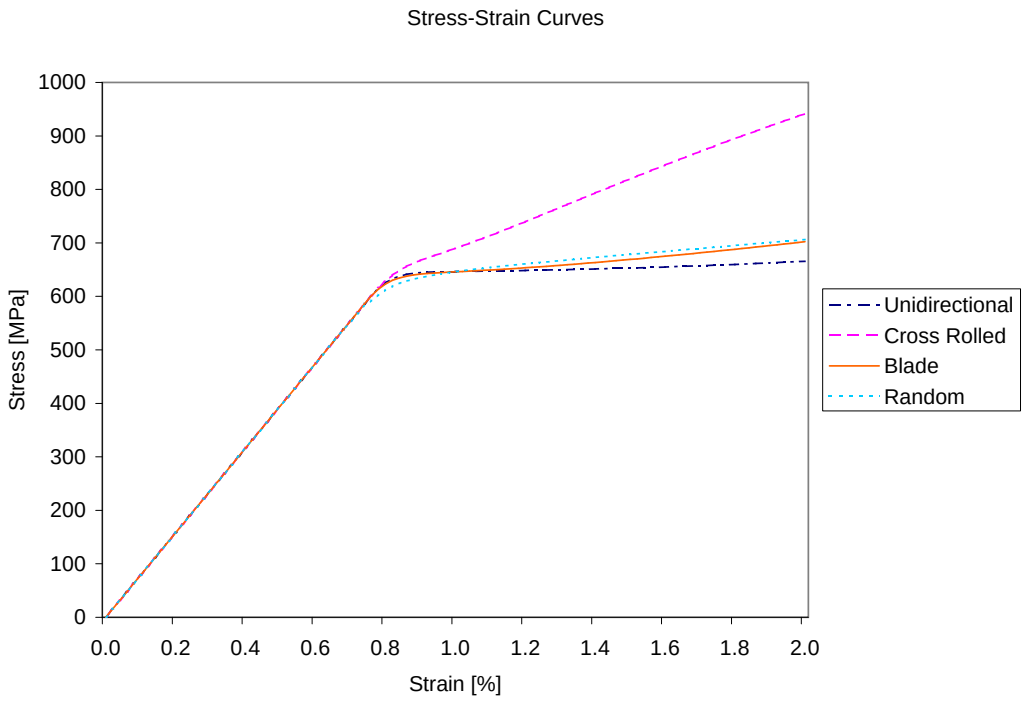

Figure A.1: Influencia de la orientación cristalográfica en el comportamiento macroscópico de la aleación Ti-6Al.

A.3 Influencia de la escala geométrica

La influencia de la escala geométrica intrínseca del material, mostrada experimentalmente en numerosas ocasiones, es recogida en el modelo a través de la dependencia geométrica de la densidad de GNDs, Ecuación A.2.

La no coincidencia de bandas de deslizamiento en los límites de grano, así como la presencia de zonas rígidas, generan deformaciones no uniformes que provocan la formación de dislocaciones. Como ya se ha explicado anteriormente, esto conlleva un endurecimiento del material. A medida que el tamaño de grano disminuye, se producen mayores gradientes que resultan en mayores pendientes de la zona plástica.

Naturalmente, este efecto es menos pronunciado a medida que crece la uniformidad de la textura, pues la falta de gradientes impide la creación de dislocaciones. La Figura A.2 muestra los resultados de los cuatro casos anteriores, para diferentes escalas.

A.4 Criterios de Fallo

La última sección se centra en el fallo del material en la presencia o ausencia de la combinación cristalográfica más desfavorable, conocida como "rogue grain". Dicha configuración incluye un grano rígido inmerso en una matriz blanda y es considerada una de las causas del fallo por "faceting" descrito al comienzo de este documento.

Un criterio de nucleación, basado en la tensión normal al plano basal, es integrado en las ecuaciones constitutivas a dos niveles, fallo independiente de puntos de integración, o fallo conjunto del elemento. Cuando dicha tensión se sobrepasa, la matriz de rigidez disminuye hasta un 95%.

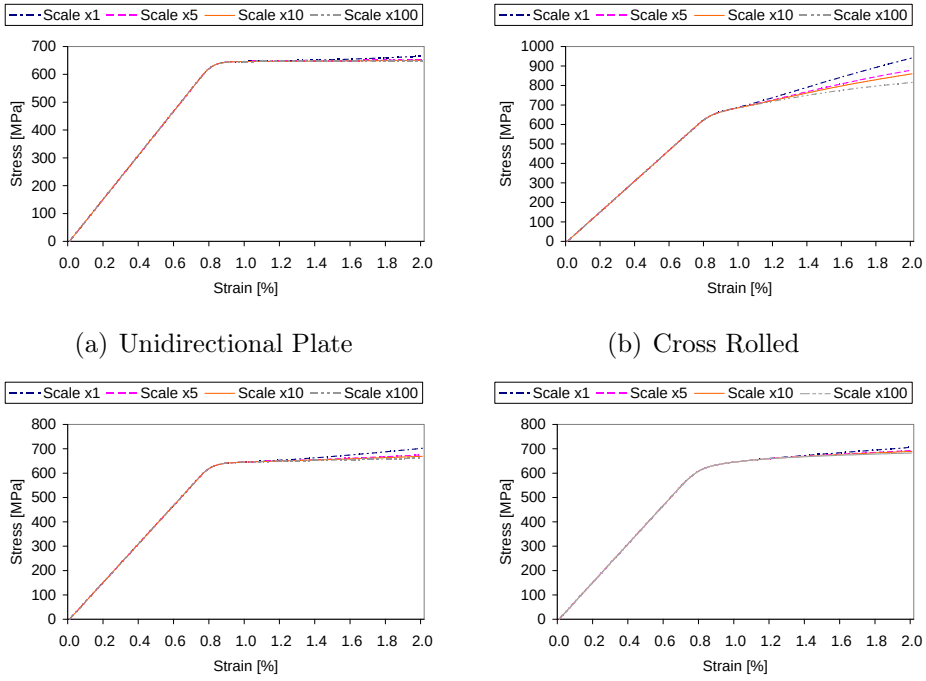

(a) Unidirectional Plate

(b) Cross Rolled

(c) Blade

(d) Random

Figure A.2: Efecto de la escala geométrica en la curva tensión-deformación de la aleación Ti-6Al.

Las simulaciones pertinentes prueban la capacidad del modelo de recoger el fallo en el lugar esperado, es decir, en el grano duro, junto al límite con la zona blanda donde se acumula mayor plastificación. El criterio, además, predice el posterior crecimiento de grieta a través los granos adyacentes tras un período de tiempo en que la carga se mantiene constante a alto nivel.

En la ausencia de esta perjudicial combinación, el criterio es modificado para predecir la rotura cuando la tensión paralela a la carga alcanza un valor crítico.

Ensayos realizados en laboratorio permiten la verificación de los resultados, que muestran una sorprendente similitud con los datos experimentales (véase Capítulo 5).

A.5 Conclusiones

Varios estudios se han llevado a cabo sobre la aleación Ti-6Al, permitiendo una mejor comprensión del comportamiento de dicho material en diferentes circunstancias. La influencia de la estructura cristalina o de la escala geométrica han sido investigadas y detalladas en el presente documento.

Igualmente, criterios de fallo que predicen la correcta nucleación y posterior crecimiento de grieta han sido desarrollados e incluidos en una subrutina UEL, del programa comercial de Elementos Finitos ABAQUS-Standard. Además, se ha confirmado la influencia de la acumulación de deformación plástica en el fallo del material, que debe ser analizada en futuros estudios.

Por otra parte, se ha encontrado una fuerte influencia del comportamiento elástico a nivel microscópico, que da lugar a muy diferentes resultados en las simulaciones realizadas. Datos experimentales son requisito indispensable para la confirmación de éste y demás resultados.

Por último, como futura línea a seguir, se ha concluído necesario el enfoque de daño no local, para así evitar los problemas de convergencia y dependencia de la malla.